ISPRS Journal of Photogrammetry and Remote Sensing 170 (2020) 174–191

Contents lists available at ScienceDirect

ISPRS Journal of Photogrammetry and Remote Sensing

journal homepage: www.elsevier.com/locate/isprsjprs

Understanding the synergies of deep learning and data fusion of multispectral and panchromatic high resolution commercial satellite imagery for automated ice-wedge polygon detection

Chandi Witharana [a,*], Md Abul Ehsan Bhuiyan [a], Anna K. Liljedahl [b,e], Mikhail Kanevskiy [b], Howard E. Epstein [c], Benjamin M. Jones [b], Ronald Daanen [d], Claire G. Griffin [c], Kelcy Kent [c], Melissa K. Ward Jones [b,e]

[a] Department of Natural Resources and the Environment, University of Connecticut, Storrs, CT, USA
[b] Water and Environmental Research Center, University of Alaska, Fairbanks, AK, USA
[c] Department of Environmental Sciences, University of Virginia, Charlottesville, VA, USA
[d] Alaska Division of Geological & Geophysical Surveys, Department of Natural Resources, Fairbanks, AK, USA
[e] Woodwell Climate Research Center, Falmouth, MA, USA

ARTICLE INFO

Keywords:
Arctic
Commercial satellite imagery
Data fusion
Deep learning
Ice-wedge polygon
Permafrost

ABSTRACT

The utility of sheer volumes of very high spatial resolution (VHSR) commercial imagery in mapping the Arctic region is new and actively evolving. Commercial satellite sensors typically record image data in low-resolution multispectral (MS) and high-resolution panchromatic (PAN) mode. Spatial resolution is needed to accurately describe feature shapes and textural patterns, such as ice-wedge polygons (IWPs) that are rapidly transforming surface features due to degrading permafrost, while spectral resolution allows capturing of land-use and land-cover types. Data fusion, the process of combining PAN and MS images with complementary characteristics often serves as an integral component of remote sensing mapping workflows. The fusion process generates spectral and spatial artifacts that may affect the classification accuracies of subsequent automated image analysis algorithms, such as deep learning (DL) convolutional neural nets (CNN). We employed a detailed multidimensional assessment to understand the performances of an array of eight application-oriented data fusion algorithms when applied to VHSR image scenes for DLCNN-based mapping of ice-wedge polygons. Our findings revealed the scene dependency of data fusion algorithms and emphasized the need for careful selection of the proper algorithm. Results suggested that the fusion algorithms that preserve spatial character of original PAN imagery favor the DLCNN model performances. The choice of fusion approach needs to be considered of equal importance to the required training dataset for successful applications using DLCNN on VHRS imagery in order to enable an accurate mapping effort of permafrost thaw across the Arctic region.

1. Introduction

Permafrost is defined as Earth materials that remain at or below 0 °C for at least two consecutive years (van Everdingen, 1998). Approximately 24% of the exposed land surface of the northern hemisphere is affected by permafrost (Brown et al., 1997), which pose challenges to infrastructure (Hjort et al., 2018) and is an integral component of what makes the Arctic natural environment unique, and especially, the region's response to climate change (Shur and Jorgenson, 2007). Thawing permafrost increases lateral exports of biogeochemical fluxes (Abbott et al., 2015, Coch et al., 2018, Levenstein et al., 2018) and alters coastal marine ecosystems, tundra geomorphology (Farquharson et al., 2019, Lewkowicz and Way 2019; Jones et al., 2019), vegetation (see Schuur and Mack 2018), and hydrology (see Lafreniere and Lamoreux, 2019). Permafrost landscapes are confronting socioeconomic development (Melvin et al., 2017; van der Sluijs et al., 2018, Raynolds et al., 2014) and rapid transition catalyzed by climate warming thawing ice-rich ground (Hinzman et al., 2005), which is challenging geosystem and ecosystem services (Vincent et al., 2017).

Ice wedges are a common permafrost subsurface feature that is

* Corresponding author.
E-mail address: chandi.witharana@uconn.edu (C. Witharana).

https://doi.org/10.1016/j.isprsjprs.2020.10.010
Received 14 January 2020; Received in revised form 14 October 2020; Accepted 19 October 2020
Available online 1 November 2020

developed by repeated frost cracking and ice-vein growth over centuries to millennia (Leffingwell 1915; Black, 1982; Mackay 1984). The growth of these wedge-shaped ice bodies is responsible for creating polygonised land surface features, i.e. ice-wedge polygons (IWPs). There are two major types of ice-wedge polygons: low-centered and high-centered (Black 1954; Britton, 1957; Hussey and Michelson, 1966; Péwé, 1975; Billings and Peterson, 1980; Everett, 1980; French, 2018). Low- and high-centered polygons have very distinctive features that can be relatively easily detected on satellite imagery and aerial photos. Low-centered polygons are framed by elevated rims that develop above actively growing ice wedges; sometimes they contain intrapolygonal ponds. High-centered polygons have elevated centers and well-developed troughs over ice wedges, often filled with water. The diameter of IWPs typically ranges from 5 m to 30 m and the associated microtopographic features, such as troughs or rims, are in sub-meter to ~1-meter scale (Black, 1982; Kanevskiy et al., 2017). Vegetation and geology maps suggest that about two-thirds or more of the Arctic landscape is occupied by polygonal ground (Raynolds et al., 2019), but the exact extent and the prevailing types of IWPs are largely unknown. The microtopography associated with IWPs affects the Arctic ecosystem from local to regional scales due to the impacts on the flow and storage of water (Liljedahl et al., 2016), vegetation and carbon (Hugelius et al., 2013; Lara et al., 2015). Over the recent decades, ice-wedge degradation has been documented at several locations across the Arctic tundra in the field and through remote sensing techniques (Jorgenson et al., 2006, Jones et al., 2015; Liljedahl et al., 2016; Steedman et al., 2017; Frost et al., 2018). Degradation of ice wedges is a quasi-cyclic process with degradation often occurring over a shorter time scale than aggradation, which tend to accumulate more organic soil (Jorgenson et al., 2015; Kanevskiy et al., 2017). The lack of knowledge on the larger geographical extent and successional stage of IWPs introduce uncertainties to regional and pan-Arctic estimates of carbon, water, and energy fluxes (Liljedahl et al., 2016; Nitze et al., 2018; Turetsky et al., 2019).

Explosion of very high spatial resolution (VHSR) commercial sensors unlocks transformational opportunities to observe, map, and document the microtopgraphic transitions associated with IWPs at multiple spatial and temporal frequencies. The entire Arctic has been imaged in 0.5 m (or even finer, 31 cm) resolution by Maxar Technologies Inc. (previously known as DigitalGlobe, Inc.) owned commercial satellite sensors on average four times in the last six years, accumulating over two petabytes of pan-Arctic image data. While these 'big' imagery repositories are freely accessible to Arctic researchers under the U.S. National Science Foundation's Office of Polar Program research awards, the imagery are still largely underutilized and derived Arctic science products are rare beyond the well-known ArcticDEM. The uses have been limited to field reconnaissance and small-scale manual/semi-automated analysis (Jones et al., 2011; Skurikhin et al., 2013, Ulrich et al., 2011, Chen et al., 2017). Both site-scale analysis based on high-resolution data (Jones et al., 2018) and landscape-scale analysis based on coarse-resolution data (Nitze et al., 2018) limit our capacity to elucidate the effect of sub-meter scale IWP degradations on regional, to pan-Arctic, to global scale processes, such as permafrost carbon climate feedback projections (Pachauri et al., 2014).

Discovery through artificial intelligence (AI), big VHSR imagery, and high performance computational (HPC) resources is just starting to be realized in Arctic science. Traditional remote sensing image classification methods fail to grapple with the sheer data volumes and inherent scene complexities involved with sub-meter spatial resolution imagery (Blaschke et al., 2014). Increasing spectral heterogeneity in VHSR imagery leads to less class variances of the conventional per-pixel based algorithms, which make difficult to accurately resolve fine-scale microtopographic features, such as IWPs (Chen et al., 2017; Abolt et al., 2019). While the geographic object-based image analysis (GEOBIA) (Blaschke 2010) competent in handling scene complexities, it is has now been flanked by the upsurge of 'big' imagery in large-scale deployments (Witharana and Lynch 2016; Lang et al., 2018; Sudmanns et al., 2019). Over the recent years, deep learning (DL) convolutional neural nets (CNNs) have secured an unprecedented dominance on computer vision applications (LeCun et al., 2015). Owing to its success in everyday image understanding, DLCNNs have now rapidly been adapted in VHSR remote sensing image analysis while superseding contemporary paradigms like GEOBIA (Zhang et al., 2016; Zhang et al., 2018; Ma et al., 2019).

The potentials of adapting cutting-edge DLCNNs from computer vision applications to remote sensing image understanding problems have been successfully demonstrated in automated mapping of shrubs (Guirado et al., 2017), whales (Guirado et al., 2019), seals (Gonçalves et al., 2020), and also IWPs (Zhang et al., 2018; Abolt et al., 2019) from VHSR imagery. DL approaches are being adapted to finely classify Arctic permafrost features from high-resolution remote sensing imagery, imagery-derived digital elevation models (DEMs), and LiDAR-based DEMs. For example, Zhang et al. (2018) demonstrated the applicability of DLCNNs to map IWPs from high-resolution aerial imagery. Abolt et al (2019) practiced a deep learning approach to extract IWPs from LiDAR-based terrain models. Jiang (2019) developed a CNN to classify Arctic wetlands from both CubeSat satellite imagery and the ArcticDEM. Huang et al (2020) have made a successful attempt to map retrogressive thaw slumps in Tibetan Plateau from CubeSat satellite imagery. Accurate delineation and classification of IWPs directly pivoted to the spatial resolution of multispectral satellite imagery (Chen et al., 2017; Zhang et al., 2018; Abolt et al., 2019). Based on a comparative analysis, Muster et al (2012) emphasized the necessity of spatial details to accurately detect and characterize IWPs and their associative microtopograpic elements, such as trough and rim. However, spectral responses of IWP features are typically poorly pronounced in imagery. Accurate detection of IWPs therefore mainly depends on multispectral imagery with high spatial (i.e. structural) details (Skurikhin et al., 2013).

Despite the palpable success and rapid adaptation of DL in remote sensing image classification, there has been very little attention paid on the possible dependency of DL model predictions on the key pre-processing steps involved in remote sensing image processing workflows. Compared to computer vision applications, in VHSR satellite image analysis, DL model predictions accuracies largely depend on the quality of the input imagery. High-level meanings (semantics) we pursue could potentially spur depending on the amount of spatial details embedded in the image (Vannucci et al., 2001). A single VHSR image scene typically covers a sizeable geographic area (~400 km^2) with highly heterogeneous semantically-complex surficial features. One of the critical pre-processing steps that is sandwiched between raw imagery and analysis-ready imagery is data fusion or commonly known as pansharpening (Witharana et al., 2014, 2016). In order to overcome technical limitations, such as saving onboard storage and optimizing the signal-to-noise ratio of incoming radiation energy, VHSR commercial satellite sensors acquire image data in a low-resolution multispectral (MS) mode and high-resolution panchromatic (PAN) mode (Ghassemian 2016; Shahdoosti and Ghassemian 2016; Li et al., 2017; Meng et al., 2019). High spatial resolution is essential to accurately describe feature shapes and textural patterns, while high spectral resolution is needed to classify thematically-detailed land-use and land-cover types (Ehlers et al., 2010; Witharana et al., 2016). Blending complementary information from PAN and MS images via pansharpening facilitates a better representation of the observed area (Wald, 2000; Ranchin et al., 2003). From a classification point of view, data fusion serves as an integral step in the processing of remotely-sensed imagery for earth and environmental applications. This is particularly true in mapping microtopographic features, such as ice-wedge polygons and their feature associations (e.g. trough, rim) (Jorgenson and Grosse 2016) that are seen in permafrost-affected landscapes, where manual and automated feature extraction hinge on the spatial details present in the imagery (Mora et al., 2015).

The central objective of this exploratory study is to systematically gauge how the spectral and spatial artifacts of the data fusion process influence the prediction accuracies of DLCNN models. Our analysis entailed a multidimensional assessment to gauge the spectral and spatial fidelities of an array of application-oriented data fusion algorithms when applied to VHSR image scenes of ice-wedge polygonal tundra. We are here presenting results from the mapping application for permafrost land environments (MAPLE, (Witharana et al., 2018; Bhuiyan et al., 2019)) framework, which is developed to extract information from big satellite imagery for Arctic science applications. MAPLE couples DLCNN algorithms with the HPC resources from the extreme science and engineering discovery environment (XSEDE, (Towns et al., 2014). The current analysis could unravel the potential predisposition of the DLCNN model to data fusion quality and landscape heterogeneity to refine automated IWP mapping at regional scales.

2. Methods

2.1. Data and study area

We selected study sites comprising sedge, barren, and tussock tundra dominant landscapes, primarily from coastal tundra region of Canada (Site 1, 25 km^2) and Wrangler Island of Russia (Site 2, 25 km^2) (Fig. 1). The candidate sites provide a substantial landscape heterogeneity for fusion algorithms to cater in the pansharpening process. The Polar Geospatial Center (PGC) at University of Minnesota provided the radiometrically corrected, orthorectified imagery, which were acquired in August 2010 by the Worldview-2 (WV2) commercial satellite sensor. The WV2 hyperspatial sensor records the panchromatic (PAN) and the eight multispectral (MS) bands with a ground sampling distance of ~ 0.46 m and ~ 1.84 m at nadir, respectively, with 11 bit radiometric resolution. Test site 1, a sedge tundra dominant wetland landscape, harbors low-centered ice wedge polygons where the polygon center is characterized typically by water impoundment. This image scene also has moist tundra, which is dominated by tussock cottongrass

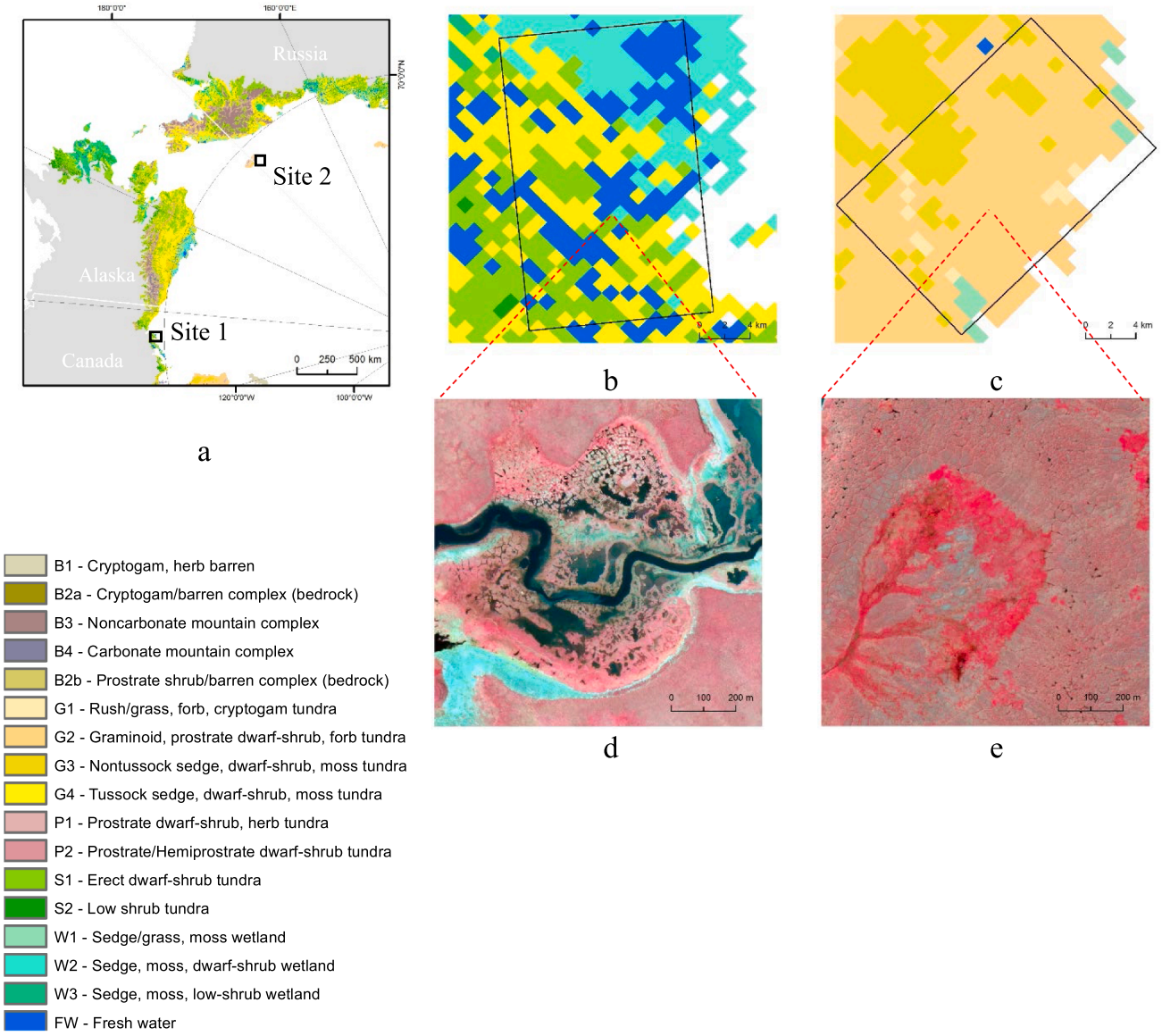

Fig. 1. Geographical setting of test study sites (a). Candidate image scenes (black hollow box) overlain by the tundra vegetation map for Site 1(b) and Site 2(c). Zoomed-in views of the candidate image scenes (d and e) as false-color composites. Tundra vegetation map and the legend are adapted from Raynold et al. 2019. Satellite imagery Copyright DigitalGlobe, Inc.

(*Eriophorum vaginatum*) and dwarf shrubs (<40 cm tall) (Raynolds et al., 2019). The WV02 scene from Wrangel Island largely encompasses the land cover class of Graminoid prostrate dwarf-shrub, forb tundra (Raynolds et al., 2019). The landscape is characterized by moist to dry tundra, with open to continuous plant cover and prostrate shrubs (<5 cm tall). The area holds cryogenic form of nano- and micro-relief, where different polygonal and spotty shapes are dominated.

2.2. Image fusion

Image fusion can occur at three different processing levels (pixel, feature, and decision) depending on the stage at which the fusion takes place (Pohl and van Genderen 1998; Alparone et al., 2007). While there is no universal way to classify fusion algorithms, studies have reported several ways to group fusion algorithms based on their design and implementation. Pohl and Van Genderen (1998) classified fusion algorithms into color-related methods and statistical/ numerical methods. Ehlers et al. (2010) considered the latter as two distinct classes (i.e. statistical and numerical) and discussed different fusion techniques under three groups as color related methods, statistical methods, and numerical methods. Ranchin and Wald (2000) and Wald (2002) proposed three ways to classify fusion algorithms: (1) the projection and substitution methods, (2) the relative spectral contribution, and (3) the method relevant to the ARSIS (a French acronym: *Amélioration de la Résolution Spatiale par Injection de Structures*, which means spatial improvement by injection structures) concept. Gangkofner et al. (2008) mainly considered the information used in a pansharpening procedure as a cursor of categorizing fusion algorithms. Their classification consists of three classes: 1) spectral substitution methods, 2) arithmetic merging, and 3) spatial-domain methods. The classification of Yakhdani and Azizi (2010) is an extension of Pohl and Van Genderen (1998), in which they identified three classes as 1) color-related techniques, 2) statistical/numerical methods, 3) Pyramid-based methods, and 4) hybrid methods.

We used eight fusion algorithms (Table 1) that are commonly encountered in the literature and incorporated into commercial remote sensing image processing software packages (e.g., ERDAS Imagine 2015) and/or open source libraries (GDAL). While providing a brief overview of candidate fusion algorithms, we encourage readers to the references listed in Table 1 for detailed descriptions on mathematical formulation and implementation of the candidate algorithms. The Brovey transform (BRV) is a straightforward spectral substitution method, which is less time- and processor-intense. Augmented versions of Brovey transform exist, such as the weighted Brovey fusion, which is the standard algorithm used by the Polar Geospatial Center (PGC) at University of Minnesota in their image pre-processing pipelines. Both algorithms fall into the first taxa (i.e. spectral substitution) of Gangkofner et al. (2008). The hyperspherical color fusion is a spectral component substitution fusion method. This is specifically designed for enhancing WorldView-2 imagery, though it is capable of fusing any multispectral imagery of three or more spectral channels. The high-pass filter (HPF) fusion is a spatial domain method (Gangkofner et al., 2008) that employs a convolution using a high-pass filter on the high resolution PAN image and then combining the filtered frequencies with the lower resolution MS image. The HPF is comparatively computationally intensive than BRV fusion. The principal component analysis (PCA) is a statistical method that transforms a multivariate dataset of correlated variables into a dataset of uncorrelated linear combinations of the original variables. The PCA methods fall into the component substitution class. The projective resolution merge (PRM) method combines high-resolution panchromatic images with lower resolution multispectral images while retaining the projective geometry used by the panchromatic data. The subtractive (SUB) fusion uses the subtractive algorithm to resolution enhance the MS image. While the SUB fusion specifically designed for IKONOS and QuickBird satellite sensors, it can be generalized to other commercial sensors as well (Ashraf et al., 2012). Both PRM and SUB fusion algorithms can be grouped into the projection and substitution taxa of Ranchin and Wald (2000). The wavelet transform (WVL) fusion, a spatial domain fusion method, extracts the high-frequency detail coefficients from the high spatial resolution PAN image and combines it with the spectral information obtained from the MS image using a combination model. All fusion algorithms were performed at their default settings to preclude the effect of the parameter optimization process on individual algorithms and to ensure an unbiased quality assessment.

Table 1
Candidate data fusion algorithms.

Algorithm	Implementation	Selected references
Brovey transform (BRV)	ERDAS Imagine	Nikolakopoulos (2008),
Hyperspherical color space (HCS)	ERDAS Imagine	Padwick et al., 2010; ERDAS Imagine 2015,
High-pass filter (HPF)	ERDAS Imagine	Gangkofner et al., 2008; Witharana et al., 2016
Principal component analysis (PCA)	ERDAS Imagine	Goforth 1998; Karathanassi et al., 2007
Projective resolution merge (PRM)	ERDAS Imagine	Lindgren and Kilston, 1996; ERDAS Imagine 2015,
Subtractive resolution merge (SUB)	ERDAS Imagine	Ashraf et al., 2012; Yang et al., 2012
Modified version of Weighted Brovey transform used by Polar Geospatial Center (PGC)	Embedded in Polar Geospatial Center's pre-processing pipeline	Amro et al., 2011; Gharbia et al., 2014
Wavelet Transform (WVL)	ERDAS Imagine	Pradhan et al., 2006; Yakhdani and Azizi, 2010

2.3. Image fusion quality evaluation

A fusion algorithm that preserves the spectral properties of the MS data and the spatial properties of the PAN data would be ideal, but there is always compromise (Witharana and Civco 2012). We corroborated both objective and subjective assessment strategies to benchmark the spectral and spatial congruency of fused products to their parent imagery (Fig. 2).

Objective quality assessments can be performed either using a direct approach or an indirect approach. The direct approach gauges the quality of the fused imagery itself. The indirect approach assesses the quality of products extracted from the fused imagery (Witharana et al., 2016). We tasked the direct approach, which involves spectral and spatial quality metrics, to gauge the quality of fused products. In our indirect approach, we used classification accuracy metrics to assess the deep learning model predictions. Tables 2 depicts the quality metrics that we used in the direct approach. Seven spectral and five spatial metrics constitute to the error budget. The most widely used metrics for evaluating spectral fidelity include; band-wise correlation (Band-CC), deviation index, peak-signal-to-noise ratio (PSNR), entropy, and mean structural similarity index (MSSIM) (Karathanassi et al., 2007, Ehlers et al., 2010; Yakhdani and Azizi 2010; Witharana et al., 2013, 2016). The MSSIM models any distortions as a combination of loss of correlation, luminance distortion, and contrast distortion. Wald (2000) proposed the ERGAS metric (from its French acronym: erreur relative globale adimensionnelle de synthese, i.e relative dimensionless global error in synthesis), which aims to provide a quick but accurate measure of the overall quality of a fused product. The spectral angle mapper (SAM) was utilized to assess the overall spectral quality of fused images (Witharana et al., 2016). Excluding two spectral metrics (ERGAS and SAM), all other metrics were calculated in band-wise manner. Our spatial fidelity metrics (Table 2) encompassed high-pass correlation (HP-CC) and edge detection using filters Canny (Canny edge CC), Sobel

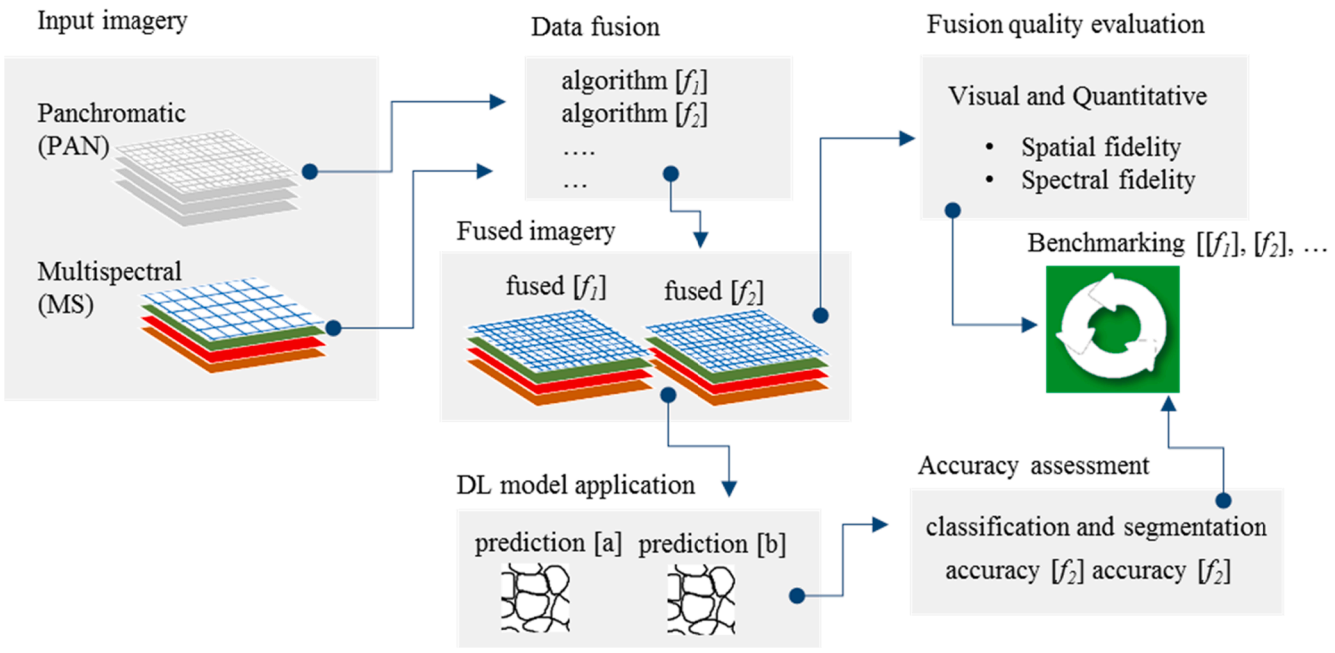

Fig. 2. A schematic of the fusion quality evaluation workflow.

(Sobel-edge RMSE), correlation between PAN and fused bands (PAN-CC), and correlation between phase congruency images of the original PAN and fused bands (Ehlers et al., 2010; Gangkofner et al., 2008; Yakhdani and Azizi 2010). Detailed discussion of an array fusion quality metrics including the ones used in this study can be found in the inclusive studies conducted by Witharana and Civco (2012), Witharana et al. (2014), Witharana et al. (2016).

Subjective fusion quality evaluation entailed two remote sensing analysts with manual image-interpretation skills to inspect the color preservation and spatial improvement of fused images with respect to their parent MS and PAN images (Fig. 2). We selected both true color (blue, green, and red) and false-color composites (green, red, and near infrared (NIR)) of candidate locations from each of the study sites for visual analysis. The color composites along with their original images were inspected by the analysts to identify spectral distortions (e.g., brightness reversions, saturation, a complete change of spectral characteristics, unnatural/artificial colors) and spatial improvement in general context. Analysts were asked to report the best two and the worst two fusion algorithms based on the spectral and spatial fidelity of the fused products. When benchmarking pansharpening quality, the analysts specifically focused on spectral and spatial clarity (e.g. edge enhancement along troughs) in relation to topographical details in fused images. Ideally, we would expect the analysts to rank order all the fused products from the best fusion algorithm to the worst fusion algorithm; however this approach is not practical because the human brain can easily discriminate extreme. Because the human brain can easily discriminate extreme variations and categorize in to limited number of cohorts (for example, the best and worst fused images) but fails to distinguish subtle variations among images with similar spectral and spatial properties (Fernandez and Wilkins 2008).

2.4. Deep learning (DL) convolutional neural net (CNN) model application

We have already trained, validated, and tested a DLCNN model to classify ice-wedge polygons from VHSR commercial satellite imagery (Bhuiyan et al., 2019). Our IWP mapping workflow centers on the Mask R-CNN model (He et al., 2017), which is an extended method for object instance segmentation. It has widely been acknowledged as a promising algorithm in semantic segmentation tasks across a multitude of scientific domains (Burke et al., 2019; Cabrera et al., 2019; Danielczuk et al., 2019; Zhang et al., 2019). The Mask R-CNN architecture is built on the Faster R-CNN (Ren et al., 2015) architecture with an additional function to predict the object masks (He et al., 2017). The Mask R-CNN is a two-stage algorithm. It first generates proposals (i.e., candidate object bounding boxes) after scanning the image and subsequently the model predicts the class, bounding box, and binary mask for each region of interest (ROI) (He et al., 2017). The primary segments of the Mask R-CNN include; backbone architecture Residual Learning network (ResNet) (He et al., 2017) for feature extraction, Feature Pyramid Network (FPN) (Lin et al., 2017) for improving representation of objects at multiple scales, and other modules, such as Region Proposal Network (RPN) for generating (RoI), RoI Classifier for class prediction of each RoI, Bounding Box Regressor (BBR) for refining RoI, and FCN (Long et al., 2015) with RoIAlign (He et al., 2017) and bilinear interpolation for predicting pixel-accurate mask. A detailed discussion on the Mask R-CNN algorithm is beyond the scope of this study and we encourage readers to refer He et al. (2017) for deeper insights on CNN architecture and the implementation.

We trained DLCCN model using hand-annotated ice-wedge polygon samples generated based on the image patches that were extracted from VHSR satellite imagery (Bhuiyan et al., 2019). We utilized ResNet-101 as the backbone of the Mask R-CNN model. The model was trained with a mini-batch size of 2 image patches (each patch with the dimension of 200 pxl × 200 xl), 350 steps per epoch, learning rate of 0.001, learning momentum of 0.9, and weight decay of 0.0001. To minimize overfitting, data augmentation was applied to introduce variability in the training data for acceptable estimation accuracy. During calibration, the weights and biases of each neuron were estimated iteratively by minimizing a mean squared error cost function using a gradient descent algorithm with back propagation. We exercised a transfer learning strategy. Pre-trained Mask RCNN was retrained using approximately 40,000 hand-annotated ice-wedge polygon samples. In the training schedule, the samples were divided into three categories of training (80%), validation (10%) and testing (10%).

The VHSR imagery used in the training phase were provided by the Polar Geospatial Center (PGC) as pansharpened 0.5 m products. The PGC uses the weighted Brovey transform as the standard data fusion algorithm in their image pre-processing workflows. In this study, we did not train the model based on training data from different fused products,

Table 2
Summary of quantitative spectral and spatial fidelity metrics.

Metric		Addressed issue/domain/expected value
Spectral	Band correlation coefficient (Band-CC)	• Quantifies the spectral correspondence between the original MS and fused images. • domain [−1,1] • As close to 1 as possible
	Deviation index (DI)	• Quantifies the normalized absolute difference of the fused image with the original MS image. • domain [0,∞) • As close to 0 as possible
	Peak signal-to-noise ratio (PSNR)	• Indicates the radiometric distortion of the fused image compared to the original MS image. • The highest possible PSNR
	Entropy	• Measures the additional information (spectral and spatial) available in the fused image compared to the original MS image. • The smallest possible entropy difference with the original MS image
	Mean structural similarity index (MSSIM)	• Reveals the spectral and structural similarity between the fused and original MS image by luminance, contrast, and structure and applying to a moving window. • domain [0,1] • As close to 0 as possible
	Spectral angle mapper (SAM)	• Pixel-wise comparison of fused image and original MS image. The value 0 indicates low resemblance while 1 indicates a high resemblance. • domain [0,1] • As close to 0 as possible
	Relative dimensionless global error in synthesis (ERGAS)	• A global indicator that calculates the amount of spectral distortion. • domain [0,∞) • Lower value (<3)
Spatial	High-pass (HP) Correlation coefficient (HP-CC)	• Quantifies the correlation between the HP filtered bands of fused image and the HP-filtered PAN image. • domain [−1,1] • as close to 1 as possible
	Phase congruency (PC) correlation coefficient (PC-CC)	• Quantifies the correlation between the PC bands of fused image and the PC of PAN image. • domain [−1,1] • as close to 1 as possible
	Panchromatic (PAN) correlation coefficient (PAN-CC)	• Quantifies the correlation between the PAN image and the fused MS image. • domain [−1,1] • as close to 1 as possible
	Root-mean-squared-error Sobel edge (Sobel-RMSE)	• Measure the average amount of spatial distortion between Sobel filtered PAN and Sobel-filtered fused image bands. • domain [,∞) • Lower value
	Canny edge correspondence (Canny Edge CC)	• A band-wise comparison of edges detected in the original PAN and the fused image. CES measured in percent. • domain [0,100]% • as close to 100 as possible

instead, we directly re-purposed the previously trained DLCNN model on the candidate fused imagery (Fig. 2). This will allow us to benchmark the prediction accuracies with respect to a single DLCNN model trained on a distinct set of hyperparameters. However, the positive or negative effect on image quality on model inferences can also be gauged with respect to the algorithm used in the fusion process. The DLCNN model prediction results from the candidate fused products were evaluated for classification accuracy and segmentation quality.

3. Results

3.1. Image fusion quality

3.1.1. Visual analysis

Figs. 3 and 5 depict examples for the representative test areas that were used in the visual evaluation. Two analysts reported the best two and the worst two fusion algorithms based on the spectral and spatial fidelity of the fused products. Tables 3 and 4 summarizes the manual benchmarking of fused imagery. With respect to spectral quality, analysts documented the HCS and WVL fusion algorithms as the best two algorithms for study sites 1 and 2. The PRM fusion reported worst spectral fidelity for both study sites, whereas the HPF and PCA fusions reported worst spectral results for the study site 1 and study site 2, respectively. Spatial quality benchmarking partly exhibited the opposite of spectral rankings. The HPF fusion showed the best spatial improvement in both study areas along with the SUB and HCS fusion algorithms. The worst spectral fidelity was shown by the WVL and PCA fusion methods. Despite the spatial details, serious color reversion can be seen in PRM fused products (Figs. 3(h) and 4(h)). In terms of spatial improvement, while the PCA (Figs. 3(f) and 4(f)) and WVL (Figs. 3(j) and 4(j)) methods maintained high degree of spectral agreement with the corresponding original MS imagery (Figs. 3(b) and 4(b)), they showed hardly any spatial improvement. Despite the resulting high contrast images show some spectral degradation, the spatial improvement of the HPF-fused imagery compensates for the losses in color fidelity. The HPF product is more visually efficient than its main contender (the HCS fusion algorithm) since it expediently signals rich visual cues to the observer to easily follow the microtopographic segmentations and undulations resulting from underlying ice-wedge network. Comparatively the HCS and SUB fusion exhibited mediocre visual quality (Figs. 3 and 4). Both BRV products showed spectral artefacts, especially over the water bodies (Fig. 3(c) and (g)).

3.1.2. Quantitative analysis

The visual evaluation was corroborated with a quantitative fusion quality budget consisting of an array of spectral and spatial indices. Figs. 8–10 and Figs. 11–13 correspond to the summarization of objective quality budget from the candidate site 1 and 2, respectively. In relation to fused imagery from study site 1, the basic spectral metric (Fig. 8) - correlation coefficient (CC) - reports the best scores for the HCS, PCA, and SUB fusion algorithms indicating discernible band-wise agreement between fused and original MS imagery. The fused product from PGC reported the lowest CC with high variability. The HPF algorithm showed CC results comparable to standard BRV fusion method. In terms of deviation index (DI) (Fig. 8), The PCA showed the worst scores with high variability. While the HCS reported the lowest DI, the HPF, PGC, and SUB fused products showed low and akin results. With respect to the peak signal-to-noise ratio (PSNR), the SUB fusion algorithm reflected the best scores followed by HCS and HPF fusion algorithms. The highest radiometric distortion was shown by the fused product from the PGC and it was comparable to the PSNR scores of standard BRV algorithm (Fig. 8). The best scores for Entropy was reported by the WVL fusion algorithm, while the highest Entropy difference was shown by the BRV fusion algorithm. Comparatively, the HCS algorithm had low entropy difference, indicating the radiometric similarity to the original MS image. The HPF methods had the least and greatest radiometric distortions, respectively. The standard BRV fusion reported the worst scores for the structural similarity measure (MSSIM) (Fig. 8). The low MSSIM indicates the loss of illumination, radiometric alteration, and contrast distortion between the fused and the original MS images. The HCS, SUB, and PGC fused products manifested high scores for the MSSIM. According to the two global measures (Fig. 8) – spectral angle mapper (SAM) and relative dimensionless global error in synthesis (ERGAS) - ,

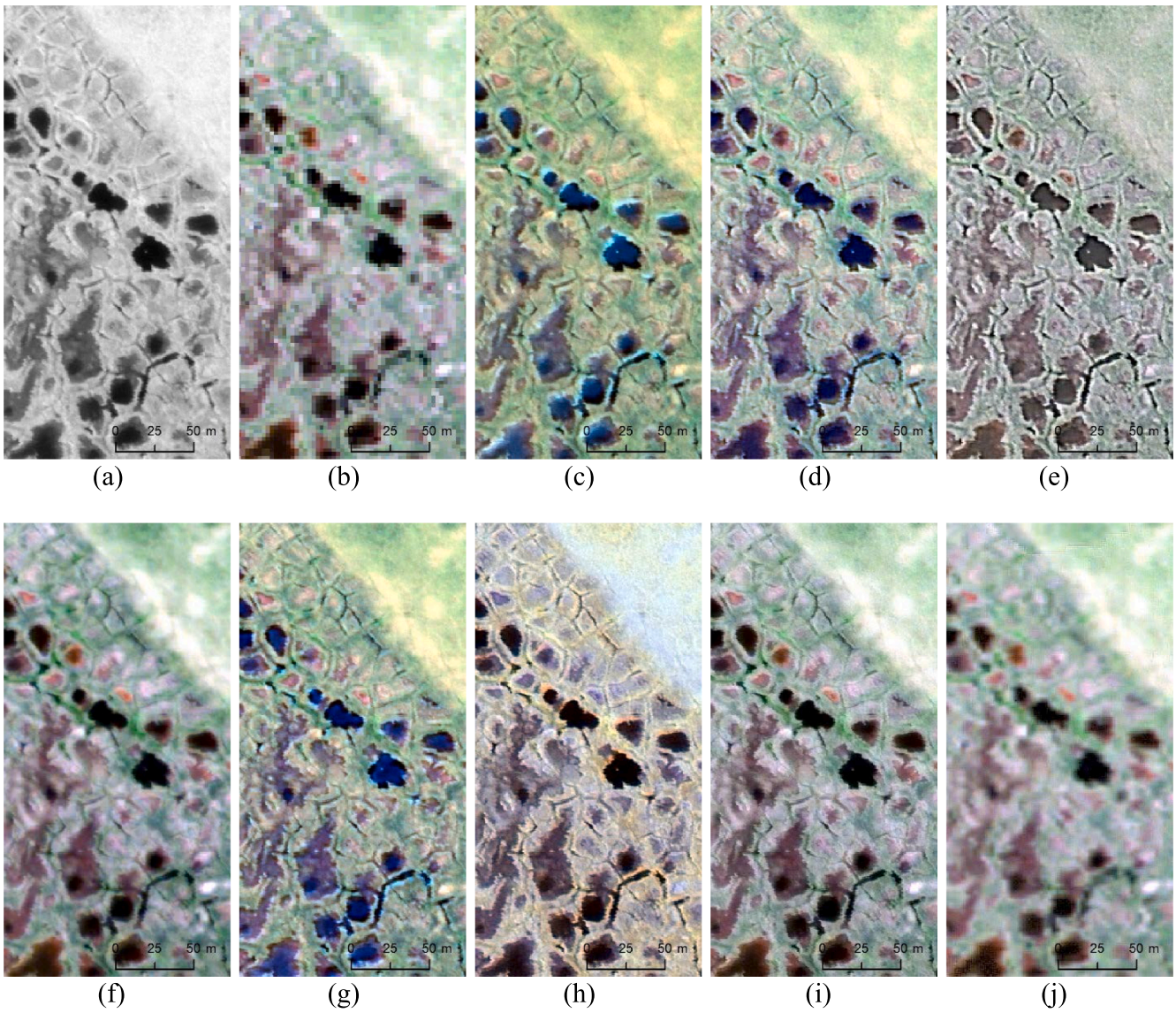

Fig. 3. Visual inspection of WV2 scene from site-1 for spectral and spatial fidelity of fused products. Original MS and fused products are shown as true color composites. (a) PAN image, (b) MS image, (c) Brovey fusion, (d) Hyperspherical color transform fusion, (e) High-pass fusion, (f) Principal component analysis fusion, (g) Fused product from PGC, (h) Projective resolution merge, (i) Subtractive resolution merge, (j) and Wavelet fusion. Satellite imagery Copyright DigitalGlobe, Inc.

Table 3
Visual benchmarking of spectral fidelity.

Test area	Spectral fidelity	
	Best	Worst
Site 1	WVL, HCS	PRM, HPF
Site 2	WVL, HCS	PRM, PCA

Table 4
Visual benchmarking of spatial fidelity.

Test area	Spatial fidelity	
	Best	Worst
Site 1	HPF, SUB	WVL, PCA
Site 2	HPF, HCS	WVL, PCA

the PRM fusion had the worst score for SAM and third worst score for the ERGAS. The BRV, PGC, PRM, and PCA fused products exhibited noticeably high scores for ERGAS, questioning the spectral authenticity of the fused imagery with respect to the original MS image. The HCS, HPF, and SUB yielded very healthy scores for the ERGAS. Both the SAM and ERGAS have disqualified BRV, PCA, PGC, and PRM products. Figs. 9 and 10 illustrate the spatial quality plots for the fused imagery from site 1. The best spatial agreement (PAN-CC) between the original PAN image and the fused product was shown by the PRM fusion algorithm. While the SUB and HCS reported the highest mean PAN-CC scores, the HPF had the third best outcome (Fig. 9). The PGC scored the worst for the PAN-CC indicating the inability of the underlying fusion algorithm to inject high frequency information from the PAN to the MS image. Likewise PAN-CC, the PGC and WVL showed the worst agreement with respect to the phase congruency (PC-CC) imagery of fused bands and the original PAN (Fig. 9). The HPF reported the highest score for PC-CC testifying its ability to maintain the same level of spatial details in the fused product. While the SUB algorithm had the best score for the high-pass filter correlation (HP-CC), the PGC product showed the worst metric values. In general, majority of fusion algorithms were able to maintain a healthy Canny edge correspondence between fused bands and original PAN image. The HPF fusion shown to be the best contender with low variability. In contrast to the Canny edge measure, the RMSE of the Sobel

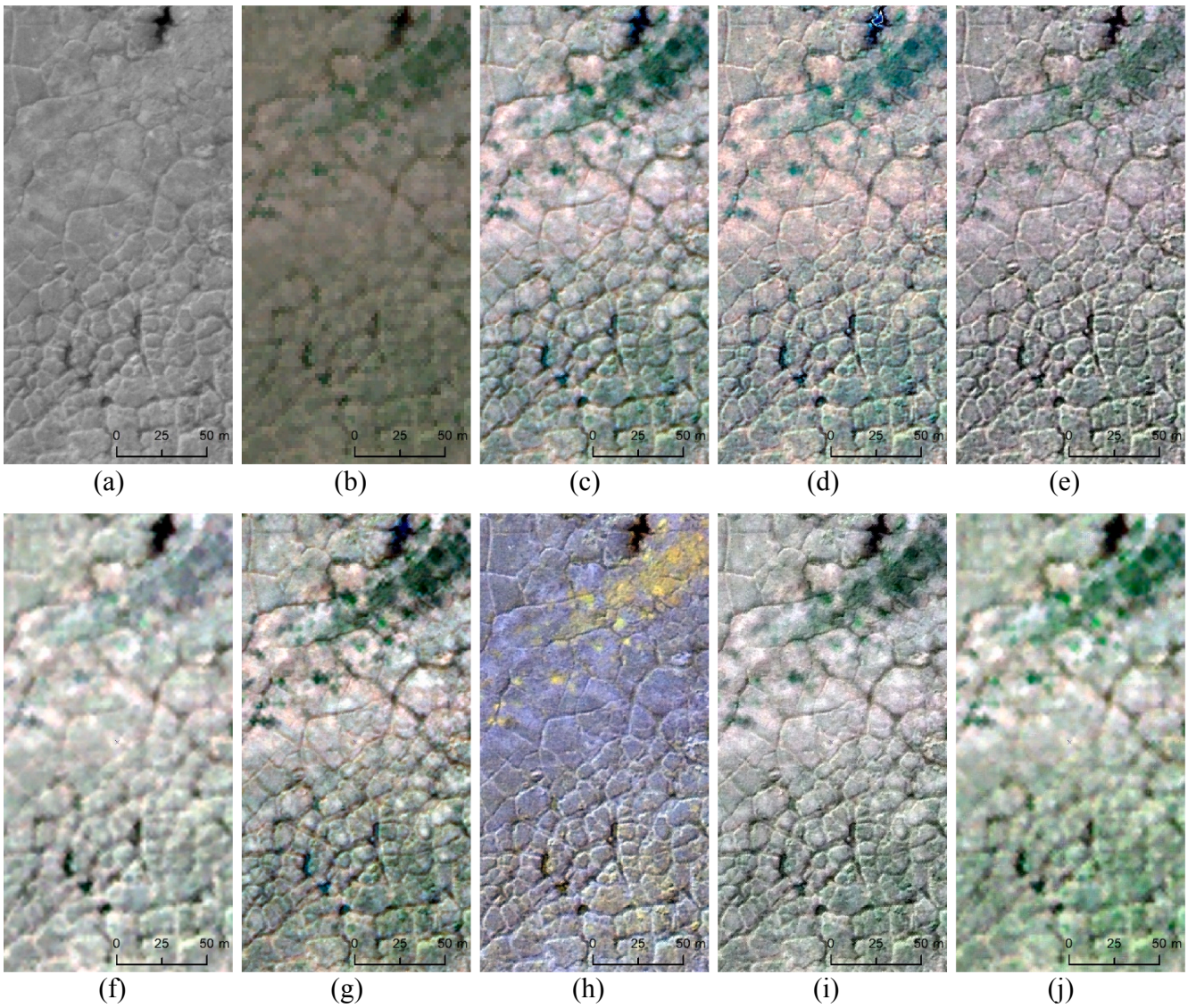

Fig. 4. Visual inspection of WV2 scene from site-2 for spectral and spatial fidelity of fused products. Original MS and fused products are shown as true color composites. (a) PAN image, (b) MS image, (c) Brovey fusion, (d) Hyperspherical color transform fusion, (e) High-pass fusion, (f) Principal component analysis fusion, (g) Fused product from PGC, (h) Projective resolution merge, (i) Subtractive resolution merge, and (j) Wavelet fusion. Satellite imagery Copyright DigitalGlobe, Inc.

edge detector has been able to accent the spatial fidelity of fused products. Evidently, the PGC product showed the worst spatial improvement whereas PRM and BRV appeared to be the promising fused products. Fig. 10 depicts a band-wise comparison of PC-CC and HP-CC for a selected subset of algorithms. This selection was based on the visual benchmarking (Table 4) of the fused imagery for the spatial quality. With respect to the PC-CC metric, the HPF showed the highest and consistent agreement across all fused bands against the original PAN image. The second best contender is the SUB fusion algorithm. Switching of ranking of HPF and SUB can be observed in relation to the HP-CC metric. Yet, the HPF fused product appeared to be the most consistent one across all bands. The worst band-wise results were reported by the PGC fused product, which was clearly inferior to even the WVL fusion algorithm.

The spectral quality budget of site 2 (Fig. 11) provides objective benchmarks for color preservation character of the candidate fused products. Similar to the observations from site 1, the PGC product reported the worst scores for the band-CC measure. The PCA and PRM had serious color distortions, which are clearly evinced in their band-CC and DI plots. Both the BRV and WVL were quality spectrally faithful in terms of band-CC; however, the BRV fusion showed high deviations scores for the DI measure. In terms of radiometric distortions, the HPF, HCS, WVL, and SUB reported high and healthy scores for the PSNR. In contrast, the PGC and BRV performed poorly. The highest structure similarity (MSSIM) between the fused and the original MS was shown by the PCA algorithm while BRV and PRM showed poor results. The SAM and ERGAS provide a global picture of all the fusion contenders. The PGC fused product performed poorly compared to the rest of the pan-sharpened products. The HPF, HCS, and SUB showed promising metric values for the both SAM and ERGAS. The summarization of spectral quality measures for the site 2 are shown in Figs. 12 and 13. The worst results for the PAN-CC were shown by the PCA and PGC fused products. The PRM shown to be the best algorithm with respect to PAN-CC (Fig. 12). The comparison results from PC-CC manifest that the HPF and SUB fusion algorithms were able to maintain high degree of spatial agreement between the fused and PAN images. Obviously, WVL and the PGC fused products provided poor-quality results. The HP-CC metric has reiterated the benchmarking of PC-CC for the PGC, PCA, and WVL fused products (Fig. 12). The HPF and SUB fusion algorithms elected to be the best contenders in terms of HP-CC. As seen in the site 1, except the PRM, all others produced high and comparable results for the Canny edge metric without providing much clues on the spatial efficacy of

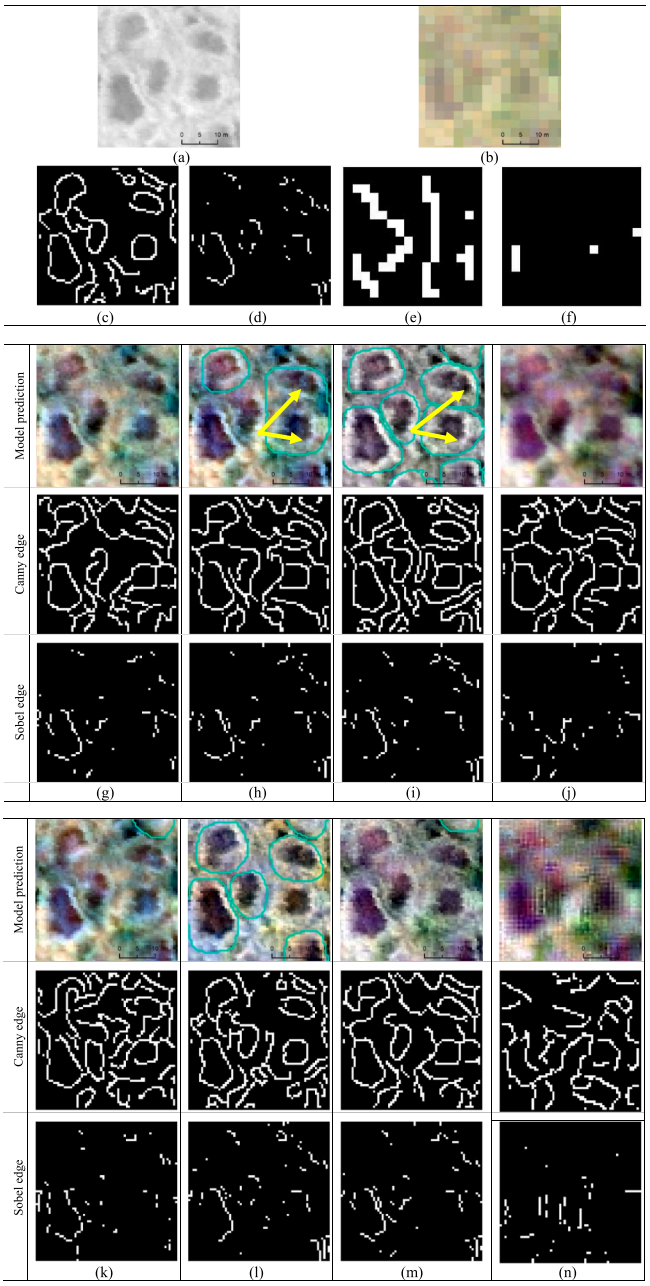

Fig. 5. Zoomed-in views from Site-1 showing edge-filtered (Canny edge detector and Sobel edge detector) images and deep learning model predictions that are shown in cyan outline on true color composites of fused imagery. (a) PAN image, (b) MS image, (c) Canny edge filtered PAN image, (d) Sobel edge filtered PAN image, (e) Canny edge filtered MS image, (f) Sobel edge filtered MS image. Edge detection and model prediction of fused products are arranged into columns with three panels for each fused product: (g) Brovey fusion, (h) Hyperspherical color transform fusion, (i) High-pass fusion, (j) Principal component analysis fusion, (k) Fused product from PGC, (l) Projective resolution merge, (m) Subtractive resolution merge, and (n) Wavelet fusion. Yellow arrows indicates example polygons seen on the image. Satellite imagery Copyright DigitalGlobe, Inc.

underlying fusion algorithms. The Sobel edge detector has testified for the poor spatial improvement associated with the PGC fused imagery (Fig. 12). As discussed under site 1, we have a selected subset of fused products based on the visual benchmarkings (Table 4) to do a band-wise comparison of PC-CC and HP-CC metrics (Fig. 13). All fused bands of the HPF fusion algorithm exhibited high and stable scores for the PC-CC and the HP –CC metrics. In contrast the PGC and WVL showed inferior results. The HP-CC values of PCA algorithm show a serious fusion artifact associated with the NIR band.

3.2. Deep learning model predictions

We applied the trained Mask-RCNN model on the fused imagery from both study sites. The model-inferred imagery were subjected to careful visual inspections and standard accuracy assessments. Figs. 5, 6, and 7 and Tables 5 and 6 pertain to the results from the qualitative and quantitative evaluations. Fig. 5 shows an example area from site 1 for the detailed visual analysis. The figure consists of original PAN and MS imagery and their edge maps based on Canny and Sobel edge detectors. Fused images are superimposed with model predictions (blue outline). Canny and Sobel edge maps are also provided for all the fused products. It should be noted that the edge maps for the fused and original MS imagery are based on the red band only. Evidently, the MS image (Fig. 5b) provides insufficient spatial details to resolve ice-wedge polygon boundaries when compared to the PAN image (Fig. 5a). The Canny and Sobel edge maps (Fig. 5c and f) of MS image further attest the necessity for the injection of high-frequency information from the PAN to the MS for an accurate outlining of ice-wedge polygons. Considering the example area, fused products of BRV, PCA, PGC, SUB, and WVL (Fig. 5 (g, j, k, m, n, respectively) have not been able to produce successful model predictions. In contrast, the HPF fused product (Fig. 5(i)) produced the best prediction results (see blue outlines). A close inspection of HCS and HPF (see yellow arrows on Fig. 5 (h and i) fused images reveal that the edge enhancement of the HPF clearly lead the DL model to conveniently locate the microtopographic discontinuity between two ice wedge polygons. However, in the HCS-fused image, the DL model was unable to resolve two polygons, instead, it ran into an under-segmentation scenario. Comparison of Sobel and Canny edge detection of fused imagery against those of PAN demonstrates the poor edge correspondence in WVL and PCA fusion methods. Similar to the site 1 (Fig. 5), a quick appraisal of PAN and MS imagery from site 2 (Fig. 6a and b) reveals the need for the edge enhancement of MS image for an accurate detection of ice wedge polygons. Successful DL model predictions were seen in the fused products of HCS, HPF, and SUB algorithms. The HPF fusion has provided substantial spatial details to the DL model to resolve trough network and connected ice-wedge polygons. This has actually prevented potential under-segmentation as seen in the HCS fused product (see yellow arrows in Fig. 6h and i). In general, BRV, PGC, and PRM exhibited poor classification results (Fig. 6g, k, l), respectively). The poor spatial improvement of the WVL and PCA fusion methods results zero detection of ice-wedge polygons. A close inspection of Canny and Sobel edge maps against those of the PAN image prompts the spatial authenticity of fused products. For example, the WVL and PCA have clearly missed the edge information from the original PAN image. While the fused products of the BRV and PGC do show some level of edge correspondence to the original PAN image; they lack the spatial arrangement of edges that is necessary for the DL model to follow in the prediction stage.

In order to understand how spatial details along with the color information guide the manual delineation of ice-wedge polygons, we asked two analysts to benchmark the fused products on the premise of comfort of discriminating the targets of interest from the background objects. Akin to fusion quality evaluation, the visual evaluation quantized fused products to the benchmarks of best and worst (Table 5). In both candidate scenes, the HPF fusion algorithm elected to be the best where as WVL along with PCA and PRM were identified as the worst fused products. Both the SUB and PGC stood as successful contenders to the HPF fusion algorithm. Fig. 7 shows one of the example areas that were used to gauge the quality manual delineations. To capture the two ends of the spectrum, outlines are provided for the best (HPF and PGC) and worst (PCA and WVL) fused products (Fig. 3b and c). The PAN image is provided as a reference (Fig. 3a) to visualize manual boundary outlining discrepancies. Direct comparison of HPF and PGC based outlines

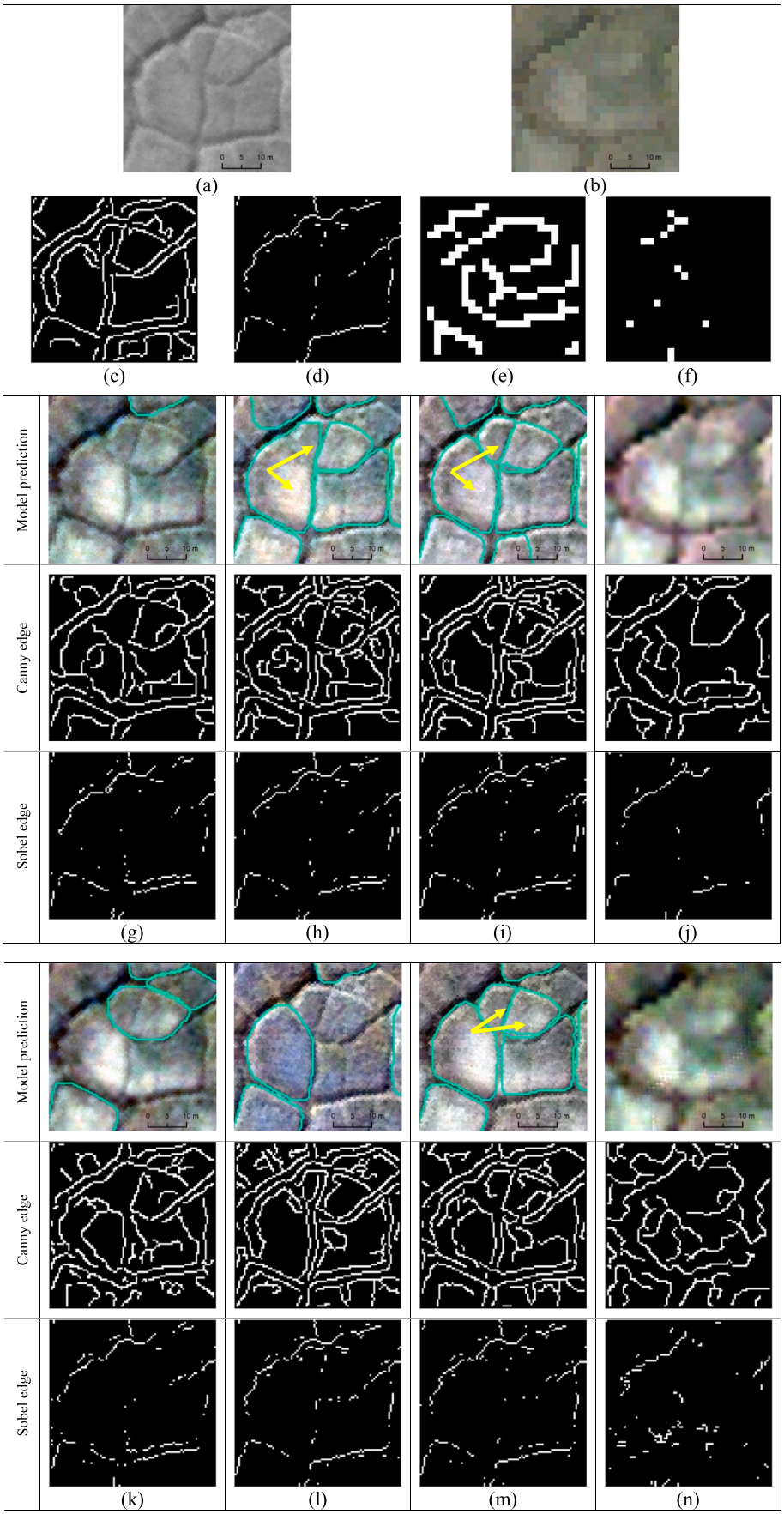

Fig. 6. Zoomed-in views of Site-2 showing edge-filtered (Canny edge detector and Sobel edge detector) images and deep learning model predictions that are shown in cyan outline on true color composites of fused imagery. (a) PAN image, (b) MS image, (c) Canny edge filtered PAN image, (d) Sobel edge filtered PAN image, (e) Canny edge filtered MS image, (f) Sobel edge filtered MS image. Edge detection and model prediction of fused products are arranged into columns with three panels for each fused product: (g) Brovey fusion, (h) Hyperspherical color transform fusion, (i) High-pass fusion, (j) Principal component analysis fusion, (k) Fused product from PGC, (l) Projective resolution merge, (m) Subtractive resolution merge, and (n) Wavelet fusion. Yellow arrows indicates example polygons seen on the image. Satellite imagery Copyright DigitalGlobe, Inc.

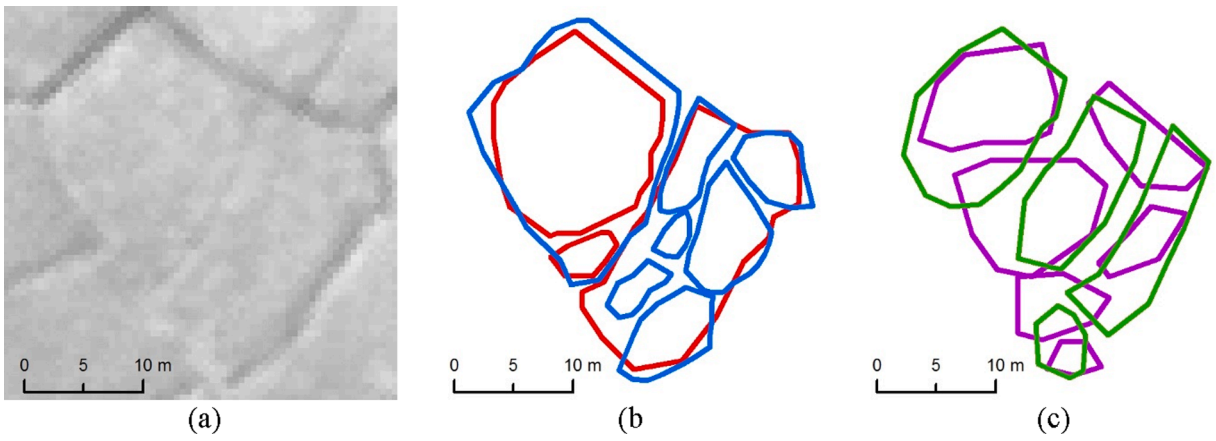

Fig. 7. Manual delineation of ice wedge polygons based on four fused products. (a) Zoomed-in view of PAN image, (b) Manual delineation based on HPF fusion (red outline) and PGC fusion (blue outline), (c) Manual delineation based on PCA fusion (green outline) and WVL fusion (magenta outline). Satellite imagery Copyright DigitalGlobe, Inc.

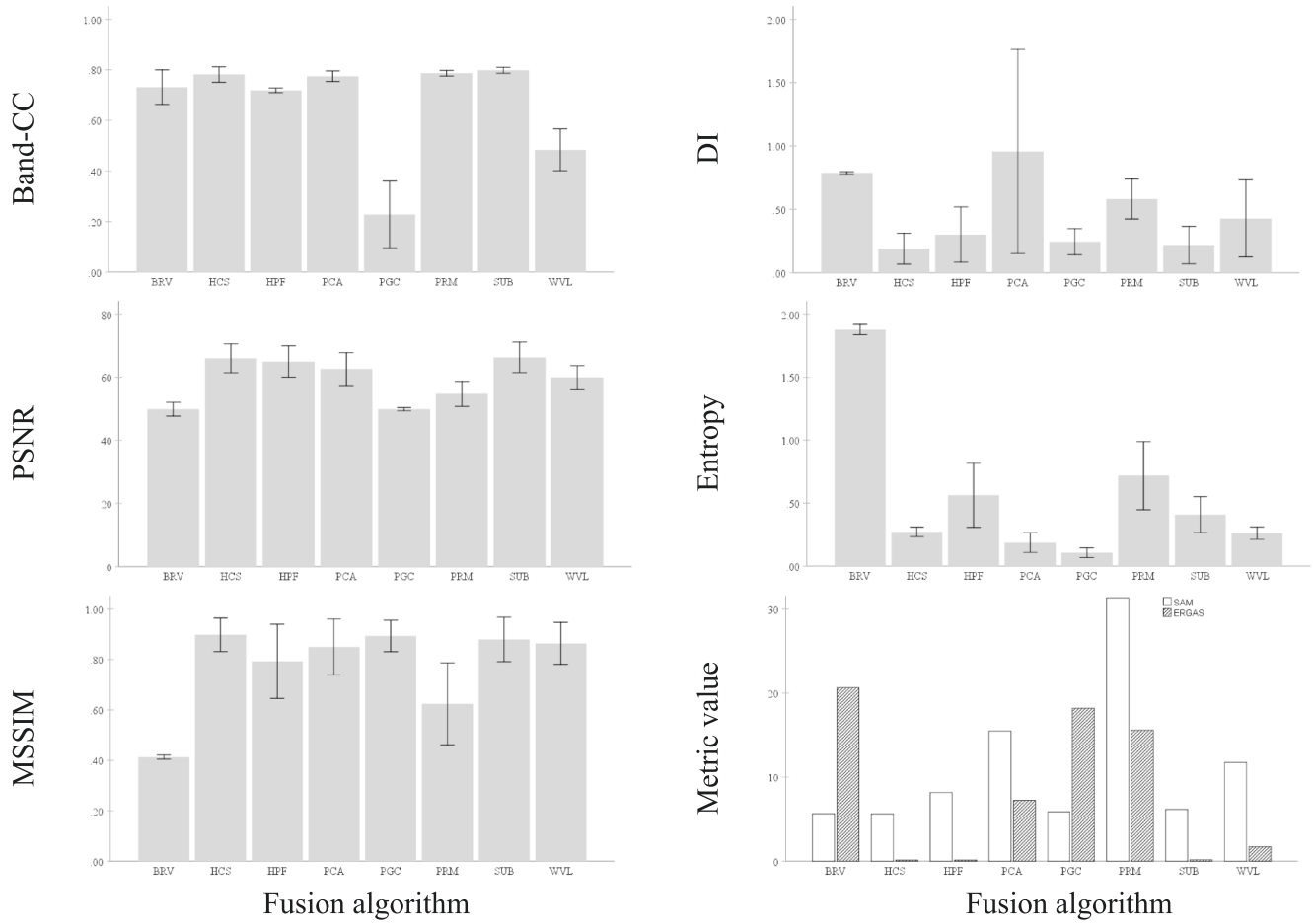

Fig. 8. Spectral quality plots for the fused imagery products of site-1. In each plot, the x and y axes depict the value of the quality metric and the candidate fusion algorithms, respectively. BRV – Brovey fusion, HCS- Hyperspherical color transform fusion, HPF- High-pass fusion, PCA- Principal component analysis fusion, PGC - Fused product from Polar Geospatial Center, PRM - Projective resolution merge, SUB - Subtractive resolution merge, and WVL – Wavelet fusion. Error bars +/- 1 SD.

(red and blue respectively) show overall agreement; however, the PGC product has misled the interpreter towards over predictions due to the synthetic ambiguity in trough network posed by fusion artefacts. Manual delineation of PCA and WVL (green and blue outlines, respectively) obviously signals the fact that the interpreter has missed spatial details in the image. Predicted boundaries are largely driven by the legacy spatial details from the MS image. Table 6 summarizes the overall accuracy of DL model predictions with respect to the fused products. In both sites, the HPF fusion has been able to maintain comparatively high accuracies. The SUB and HCS showed an upswing in their accuracies moving from site 1 to 2. The PGC maintained low and stable accuracies. In agreement with fusion quality and manual detectability, both PCA and WVL lead to worst accuracies in the group.

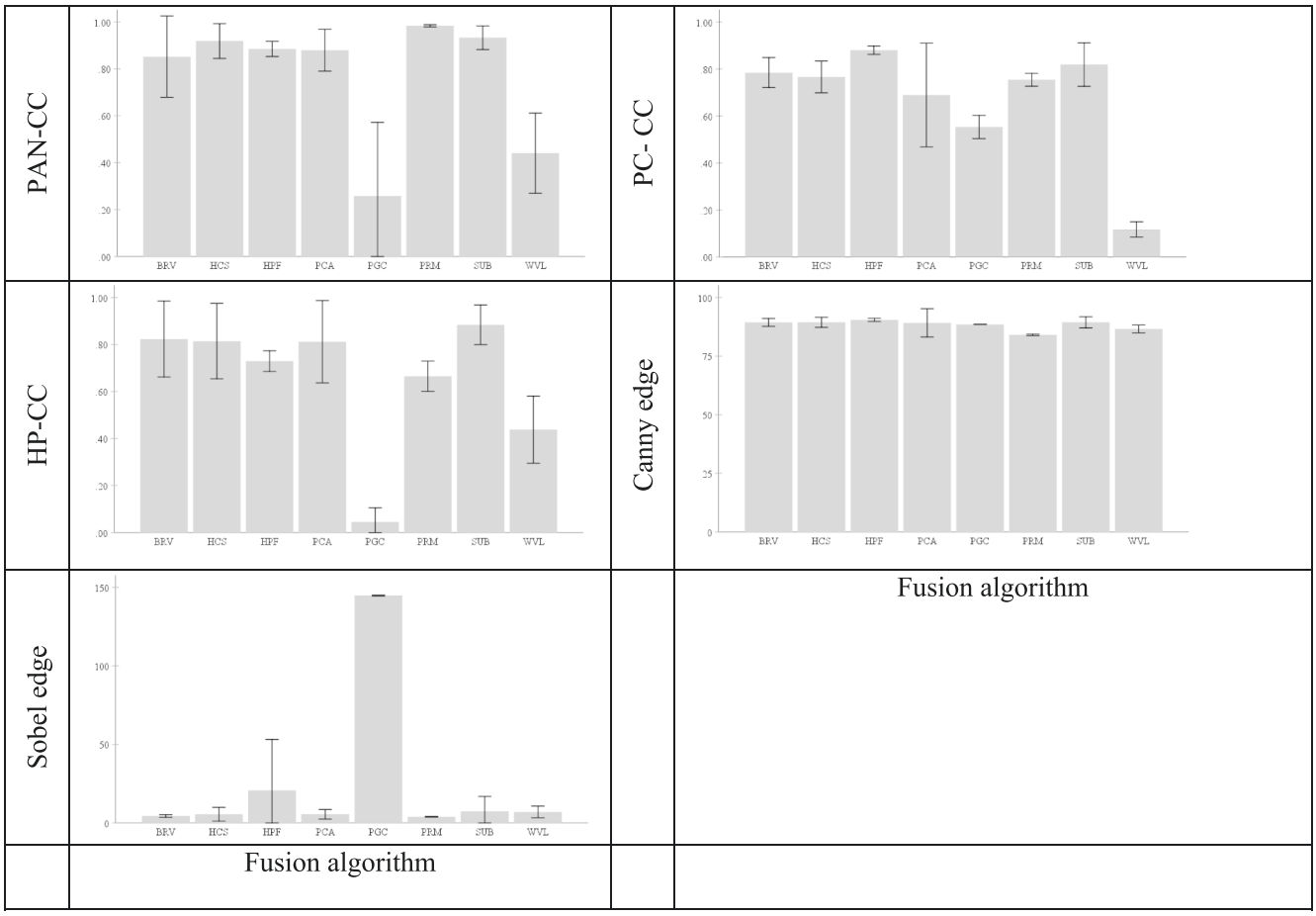

Fig. 9. Spatial quality plots for the fused products of site-1. In each plot, the x and y axes depict the value of the quality metric and the candidate fusion algorithms, respectively. BRV – Brovey fusion, HCS- Hyperspherical color transform fusion, HPF- High-pass fusion, PCA- Principal component analysis fusion, PGC - Fused product from Polar Geospatial Center, PRM - Projective resolution merge, SUB - Subtractive resolution merge, and WVL - Wavelet fusion. Error bars +/- 1 SD.

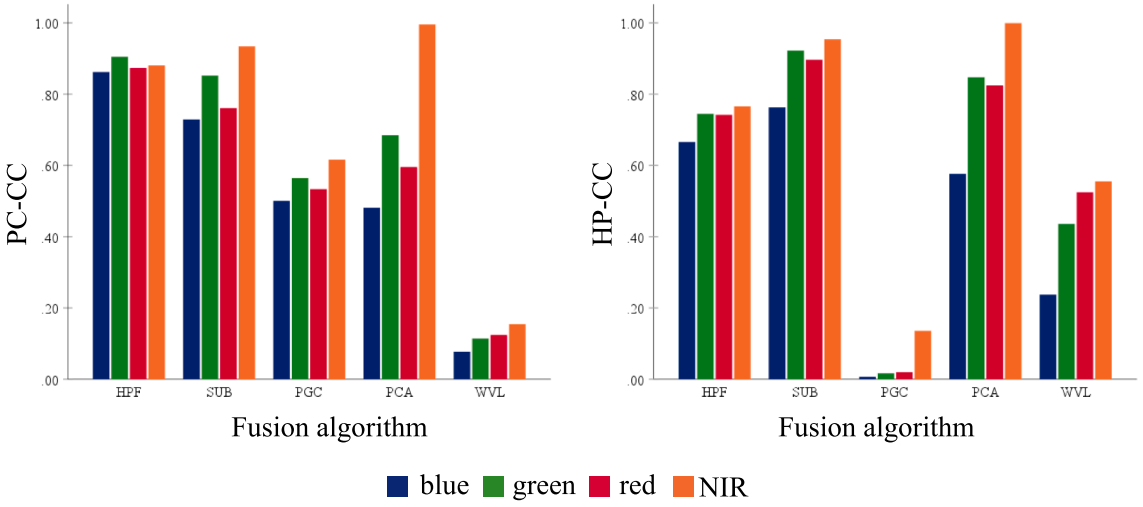

Fig. 10. A band-wise comparison for site-1. Correlation of fused and original PAN imagery for two spatial metrics; phase congruency and high-pass filtering. In each plot, the x and y axes depict the value of the quality metric and the candidate fusion algorithms, respectively. BRV – Brovey fusion, HCS- Hyperspherical color transform fusion, HPF- High-pass fusion, PCA- Principal component analysis fusion, PGC - Fused product from Polar Geospatial Center, PRM - Projective resolution merge, SUB - Subtractive resolution merge, and WVL - Wavelet fusion.

4. Discussion

Here we report the first exploratory study probing into an overlooked, but yet important aspect that is relevant to the successful adaptation of deep learning convolutional neural net (DLCNN) in very high spatial resolution (VHSR) satellite image analysis. Scene

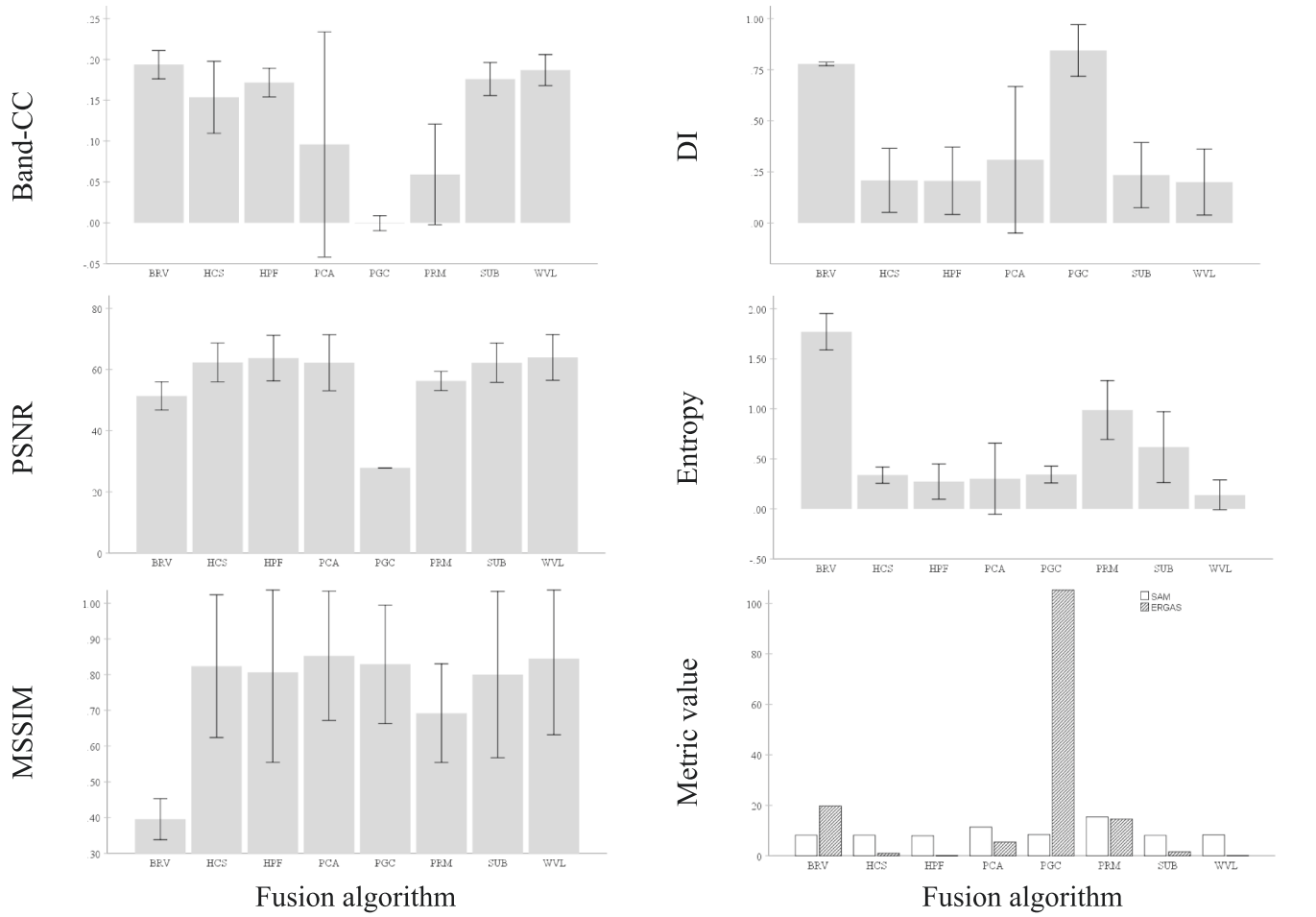

Fig. 11. Spectral quality plots for the fused imagery products of site-2. In each plot, the x and y axes depict the value of the quality metric and the candidate fusion algorithms, respectively. BRV – Brovey fusion, HCS- Hyperspherical color transform fusion, HPF- High-pass fusion, PCA- Principal component analysis fusion, PGC - Fused product from Polar Geospatial Center, PRM - Projective resolution merge, SUB - Subtractive resolution merge, and WVL – Wavelet fusion. Error bars +/- 1 SD.

dependency of fusion algorithms impedes the transferability of the knowledge on their performances across application domains. This is especially true for synthesis of imagery across large geographic areas (e.g. circumpolar mapping applications) where landscape heterogeneity can steer the performances of fusion algorithms.

The fundamental trait of imagery that unlocks the permafrost features like ice-wedge polygons is the high-spatial frequencies recorded in the PAN imagery. As seen in close-up views (Figs. 3–6), the MS imagery alone just provide a broader context but fail to morphometrically pronounce the polygonal landscape into individual units. Vice versa, the PAN imagery alone are deficient to capture nuance spectral characteristics among different ice wedge polygon types. This demands for a delicate blending of high frequencies from PAN with MS imagery. Comprehensive quantitative evaluation in conjunction with visual gauging of fusion algorithms is therefore necessary to identify those techniques that are optimal with respect to the practical implementation. Visual assessment of fusion results confer that not all fusion algorithms behave consistently across landscape variations. For example, presence of low-centered ice-wedge polygon with water impoundments in polygon centers (sedge tundra) influence the performances of fusion algorithms compared to dry tundra regions. Landscape dependency of fusion algorithms is important to consider in pan-Arctic scale ice-wedge polygon mapping applications. The HPF fusion algorithm exhibited degraded spectral quality in site 1, which is dominated by water surfaces. In contrast, the HCS fusion algorithm was able to preserve the spectral characters of the MS imagery while substantially improving the spatial details in both study sites. From the viewpoints of both subjective and objective evaluations, no single algorithm was able to produce superior results by simultaneously preserving spectral and spatial properties of the original MS and PAN images. Visual rating of fusion quality agrees with the quantitative quality budget. Despite their promising spectral quality budget, algorithms such as WVL, PCA, BRV, performed poorly with respect to spatial metrics. For instance, the WVL fusion reported competitive scores for the measures like PSNR, Entropy, and ERGAS (Figs. 8 and 9) at the serious expense of spatial fidelity. This elucidates the fact that the modelled image has gained almost zero benefit from the high-frequencies of the PAN image. These observations are comparable with the previous studies, such as Ehlers et al (2010), Kim et al (2011), and Witharana et al. (2013). Besides obtaining an overall picture on the performances of fusion algorithms in relation to permafrost mapping applications, we also wanted to eventuate potential challenges associated with the types of pansharpening approach used for image products, such as the weighted Brovey fusion algorithm. Based on our analysis, the current Brovey algorithm based products from the PGC is in acceptable quality for general image analysis purpose, such as manual interpretations and more localized semi/automated analysis. However, the spectral and spatial authenticity and, most importantly, the impact on proceeding analysis steps are questionable. Our quantitative spectral and spatial quality budget with DLCNN approaches (Figs. 8–13) places the PGC's fused product in a low rank. The Brovey fusion algorithm taxonomically falls into the category of simple spectral substitution, which generally yield good visual quality at the expense of degraded radiometric and spatial distortions (Klonus and Ehlers, 2007; Karathanassi et al., 2007; Gangkofner et al., 2008). Due to the spectral

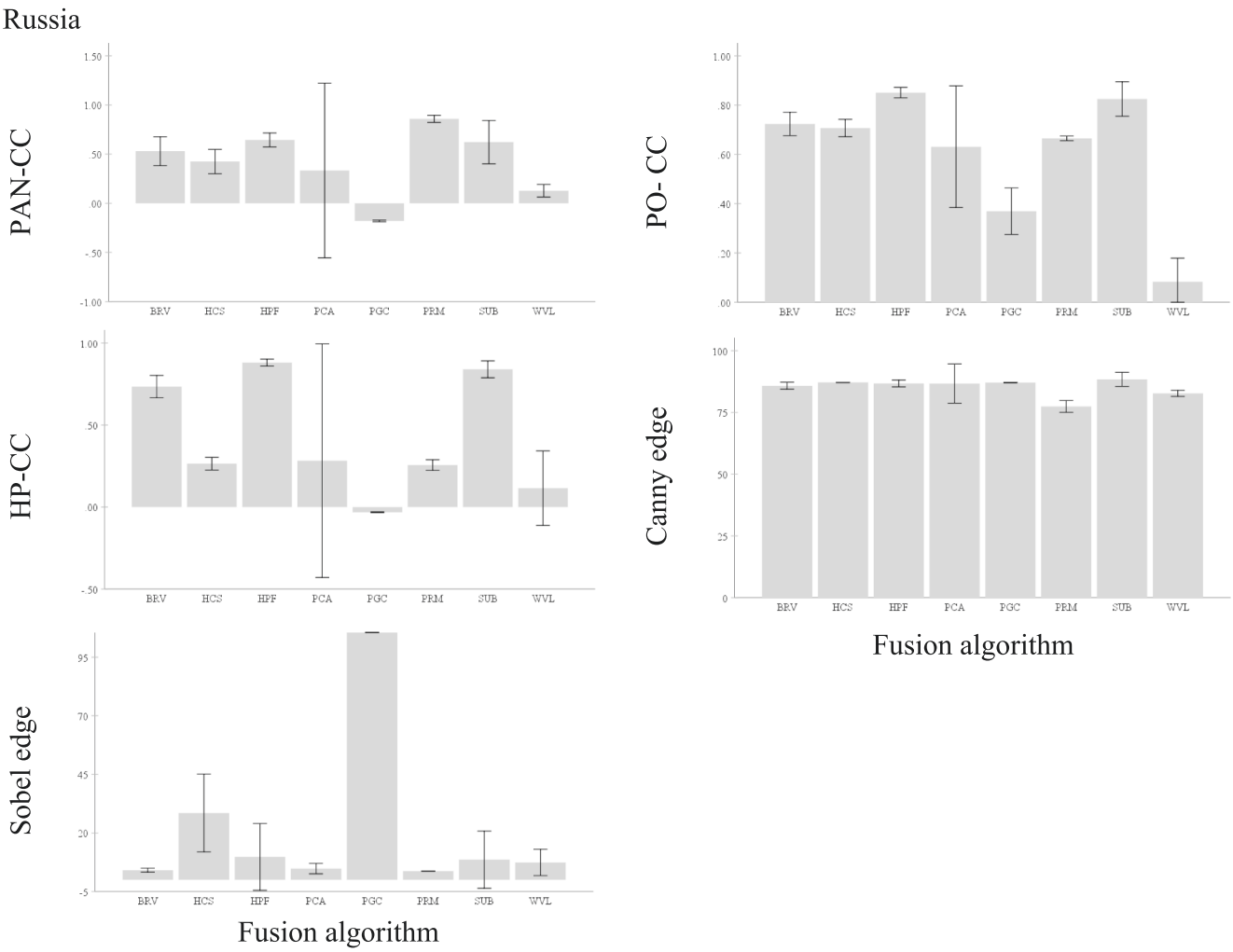

Fig. 12. Spatial quality plots for the fused products of site-2. In each plot, the x and y axes depict the value of the quality metric and the candidate fusion algorithms, respectively. BRV – Brovey fusion, HCS- Hyperspherical color transform fusion, HPF- High-pass fusion, PCA- Principal component analysis fusion, PGC - Fused product from Polar Geospatial Center, PRM - Projective resolution merge, SUB - Subtractive resolution merge, and WVL - Wavelet fusion. Error bars +/- 1 SD.

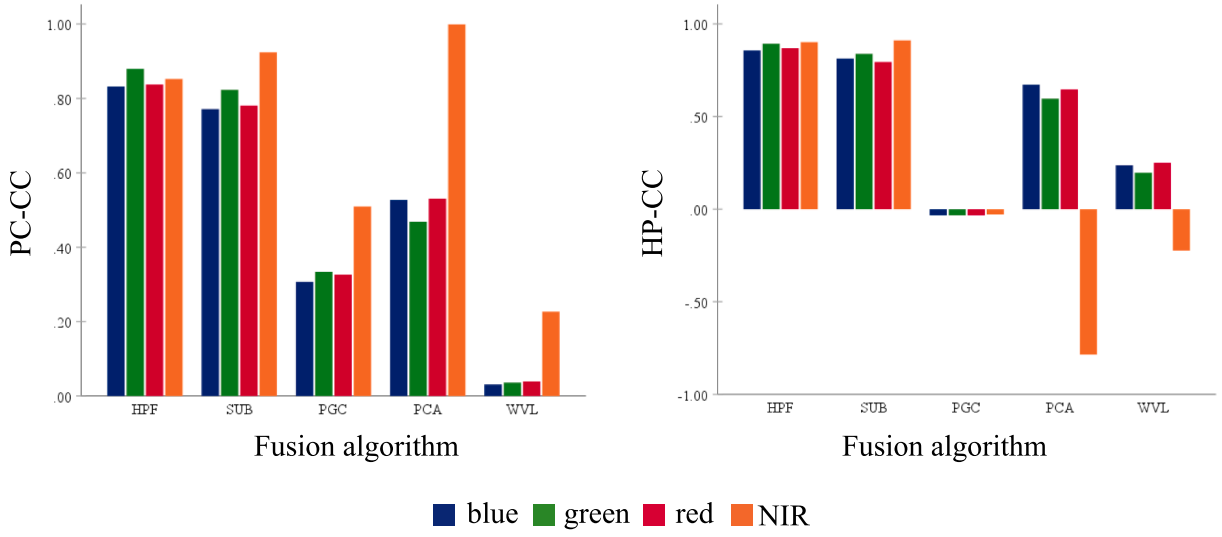

Fig. 13. A band-wise comparison for site-2. Correlation of fused and original PAN imagery for two spatial metrics; phase congruency and high-pass filtering. In each plot, the x and y axes depict the value of the quality metric and the candidate fusion algorithms, respectively. BRV – Brovey fusion, HCS- Hyperspherical color transform fusion, HPF- High-pass fusion, PCA- Principal component analysis fusion, PGC - Fused product from Polar Geospatial Center, PRM - Projective resolution merge, SUB - Subtractive resolution merge, and WVL - Wavelet fusion.

Table 5
Visual evaluation of the manual detectability ice-wedge polygons.

Test area	Detectability	
	Best	Worst
Site 1	HPF > SUB	PRM > WVL
Site 2	HPF > PGC	PCA > WVL

Table 6
Summary of deep learning classification accuracy with respect to fused imagery.

Fusion algorithm	Overall accuracy	
	Site 1	Site 2
BRV	0	18.5
HCS	43.3	70.3
HPF	80.0	74.1
PCA	0	0
PGC	36.7	33.3
PRM	70	66.7
SUB	43.3	62.9
WVL	0	0

normalization step in BRV-based approaches, the brightness values can be changed substantially affecting the histograms of the image bands (Vijayaraj et al., 2006). Our contention is that regional-scale mapping applications that sits on deep learning or other automated methods would benefit from multiple data fusion techniques. Overall, the HPF, HCS, SUB exhibited superior performances than Brovey. Despite of the subjectivity of visual analysis, our premise is that the human perception inherits the most integrated mechanisms that include spectral and spatial criteria for benchmarking fusion results. The visual inspections have elected the HPF method as one of the best contenders for manual delineation of ice-wedge polygons, while the objective metrics report noticeable disturbances to the spectral response. Visibility of important information and information saliency are the key ingredients in the manual quality assessment (Garcia et al., 2012). The HPF-pansharpened images provided the optimal visual grammar (Aksoy and Cinbis 2010) to accurately extract the ice-wedge polygons from the fuzzy background. Barten (2003) noted that in the human visual system, objects can generally be better distinguished in image from each other or from their background, especially, if the difference in luminance (or the contrast) is large. Ascending ranking of HPF, HCS, and SUB fusion algorithms, it is apparent that the HPF resorts the highest contrast for the ice-wedge polygons. Detailed psychophysical and psychological studies, such as O'Shea et al (1994); Tsushima et al. (2014), and Tsushima et al. (2016) report that spatial resolution greatly correlates with depth sensation and higher resolution enables stronger depth sensation, via that sense the realness of the image. When translating these findings to our experimental results, analysts favored the high-contrast fused products since those provided the key visual grammar - depth sensation - associated with the microtopography.

An important facet of our experiment is to assess how the quality of data fusion affect the DLCNN model predictions. Given the success of DLCNN in computer vision applications one could argue that, by design, deep networks are able to handle image quality variations since the hidden layers can digest the higher-level abstractions progressively from the low-level motifs (LeCun et al., 2015). Moreover, additional data augmentation procedure, such as mirroring, synthetic noise, and rotations can leverage the DLCNN model's immunity to image perturbations. We remit the point that providing good quality images could potentially improve the efficacy of the DLCNN classifications. Alterations originating from the fusion process directly disturb the quality of the imagery funneling to the DLCCN model. Visual evaluations and quantitative assessments assert the link between fusion quality and DLCCN model predictions (Tables 5 and 6, Figs. 4 and 5). The DLCNN model was trained based on the hand annotated training samples are based on the pansharpened imagery of the Brovey fusion algorithm. This can spontaneously trigger the notion that better classification results should come from fused products of Brovey fusion algorithm than those of either HPC or HCS fusion algorithms. However, improved spatial resolution with preserved spectral details lead the DLCNN to accurately resolve ice-wedge polygons from the fused images of HPF and HCS. One reason behind the low immunity of the DLCNN model to landscape variations could be the quality of the pansharpened imagery. It is generally expected that the DLCNN model could face difficulties when moving from one landscape regime to another, for instance from sedge tundra to tussock dominant or to graminoid tundra, partly because of the confinement of training samples to certain locale. Expanding the repository of training samples to capture the landscape variability across a large geographic domain is extremely time and labor prohibitive. Similarly, leveraging the quality of pansharpened imagery could substantially improve the DLCNN model's elasticity to different tundra units. Although we have tested an array of fusion algorithms, we admit that there are other fusion methods, such Graham Schmidt fusion (Laben et al., 2000), University of New Brunswick fusion (Zhang 2002), and Ehlers fusion (Ehlers et al., 2010), which are proven to be successful in different application domains (Witharana et al., 2013, 2016) and that may further improve mapping efforts of IWPs.

Application of VHSR commercial satellite imagery for addressing transdisciplinary research challenges in Arctic sciences has been gaining a fast attention over the last few years. Despite the luxury of free access to sheer volumes of commercial imagery, the best practices and workflows for handling VHSR imagery for circumpolar applications are still at early stages. Rapid uptake of DLCNN approaches in VHSR satellite image analysis is posing new frontiers in modern remote sensing. Findings from our systematic analysis posits the scene dependency of fusion algorithms and the need for careful selection of the appropriate algorithm for the classification problem in hand, or alternatively, recommend the use of multiple algorithms for large regional applications. Such gradation of best mapping practices would be of great interest in other permafrost feature mapping such as frost boils, pingos, baydzherakhs, retrogressive thaw slumps. Continued consideration of fusion algorithms and training dataset selection and size can guide Arctic researchers to more effectively exploit the VHSR commercial imagery in domain-specific applications.

5. Conclusion

There is an emerging need for establishing best practices and workflows for handling very high spatial resolution (VHSR) satellite imagery for pan-Arctic applications. Our study highlights the potential effects of data fusion algorithms on the deep learning convolutional neural net (DLCNN) model predictions accuracies for pan-Artic ice-wedge polygon tundra mapping. In addition to advancing our knowledge on the performances of fusion algorithms in relation to permafrost mapping applications, another important fact that we wanted to eventuate is the potential challenges associated with the pansharpened image products that are derived from the weight Brovey fusion algorithm. Based on our analysis, the Brovey algorithm based products, such as from the Polar Geospatial Center, are in acceptable quality for general image analysis purpose. However, the spectral and spatial authenticity and, most importantly, the impact on proceeding analysis steps are questionable. Overall, our experimental results posit the scene dependency of fusion algorithms and the need for careful selection of the appropriate algorithm for the classification problem in hand, without limiting to ice-wedge polygon mapping but also other VHSR imagery enabled permafrost feature mapping applications.

Declaration of Competing Interest

The authors declare that they have no known competing financial interests or personal relationships that could have appeared to influence

the work reported in this paper.

Acknowledgments

This work was supported by the Arctic System Science program at the U.S. National Science Foundation's Office of Polar Programs (NSF-OPP) awards 1720875 and 1722572. Supercomputing resources were provided by the Extreme Science and Engineering Discovery Environment (XSEDE) under National Science Foundation grant number ACI-1548562. Satellite imagery satellite imagery was provided by the Polar Geospatial Center under NSF-OPP awards 1043681 and 1559691. Authors would like to thank Torre Jorgenson and Yuri Shur for their insights on permafrost feature classification. Authors also would like to thank Amber Agnew for hand-annotated training data production.

References

Abbott, B.W., Jones, J.B., Godsey, S.E., Larouche, J.R., Bowden, W.B., 2015. Patterns and persistence of hydrologic carbon and nutrient export from collapsing upland permafrost. Biogeosciences 12 (12), 3725–3740.

Abolt, C.J., Young, M.H., Atchley, A.L., Wilson, C.J., 2019. Brief communication: Rapid machine-learning-based extraction and measurement of ice wedge polygons in high-resolution digital elevation models. The Cryosphere 13 (1), 237–245.

Alparone, L., Wald, L., Chanussot, J., Thomas, C., Gamba, P., Bruce, L.M., 2007. Comparison of Pansharpening Algorithms: Outcome of the 2006 GRS-S Data-Fusion Contest. IEEE Trans. Geosci. Remote Sens. 45 (10), 3012–3021.

Aksoy, S., Cinbis, R.G., 2010. Image Mining Using Directional Spatial Constraints. Geosci. Remote Sens. Lett., IEEE 7, 33–37.

Amro, I., Mateos, J., Vega, M., Molina, R., Katsaggelos, A.K., 2011. A survey of classical methods and new trends in pansharpening of multispectral images. EURASIP J. Adv. Signal Process. 2011 (1), 79.

Ashraf, S., Brabyn, L., Hicks, B.J., 2012. Image data fusion for the remote sensing of freshwater environments. Appl. Geogr. 32 (2), 619–628.

Barten, P.G., 2003. Formula for the contrast sensitivity of the human eye. Electronic Imaging 2004, 5294. SPIE.

Bhuiyan, M.A.E., Witharana, C., Liljedahl, A.K., 2019. Big Imagery as a Resource to Understand Patterns, Dynamics, and Vulnerability of Arctic Polygonal Tundra. AGU Fall Meeting 2019, San Francisco, CA.

Billings, W.D., Peterson, K.M., 1980. Vegetational change and ice-wedge polygons through the thaw-lake cycle in Arctic Alaska. Arct. Alp. Res. 12 (4), 413–432.

Black, R.F., 1982. Ice-Wedge Polygons of Northern Alaska. In: D.R. Coates (Ed.), Glacial Geomorphology: A proceedings volume of the Fifth Annual Geomorphology Symposia Series, held at Binghamton New York September 26â€“28, 1974. Springer Netherlands, Dordrecht, pp. 247–275.

Black, R.F., 1954. Permafrost – a review. Bull. Geolog. Soc. Am. 65, 839–858.

Blaschke, T., Hay, G.J., Kelly, M., Lang, S., Hofmann, P., Addink, E., Queiroz Feitosa, R., van der Meer, F., van der Werff, H., van Coillie, F., Tiede, D., 2014. Geographic Object-Based Image Analysis â€“ Towards a new paradigm. ISPRS J. Photogramm. Remote Sens. 87, 180–191.

Blaschke, T., 2010. Object based image analysis for remote sensing. ISPRS J. Photogramm. Remote Sens. 65 (1), 2–16.

Britton, M.E., 1957. Vegetation of the Arctic tundra. In: Hansen, H.P. (Ed.), Arctic Biology: 18th Biology Colloquium. Oregon State University Press, Corvallis, pp. 26–61.

Brown, J., Ferrians Jr, O.J., Heginbottom, J.A., Melnikov, E.S., 1997. Circum-Arctic Map of Permafrost and Ground-Ice Conditions (National Snow. and Ice Data Center/ World Data Center for Glaciology, Boulder CO.

Burke, C.J., Aleo, P.D., Chen, Y.-C., Liu, X., Peterson, J.R., Sembroski, G.H., and Lin, J.Y.-Y., 2019, Deblending and Classifying Astronomical Sources with Mask R-CNN Deep Learning: Monthly Notices of the Royal Astronomical Society.

Cabrera, C., Cervantes, D., MuÃ±oz, F., Hirata, G., JuÃ¡rez, P., and Flores, D.-L., 2019, Mask R-CNN to Classify Chemical Compounds in Nanostructured Materials. In: Latin American Conference on Biomedical Engineering, Springer, pp. 401–411.

Coch, C., Lamoureux, S.F., Knoblauch, C., Eischeid, I., Fritz, M., Obu, J., Lantuit, H., 2018. Summer rainfall dissolved organic carbon, solute, and sediment fluxes in a small Arctic coastal catchment on Herschel Island (Yukon Territory, Canada). Arct. Sci. 4 (4), 750–780.

Chen, Z., Pasher, J., Duffe, J., Behnamian, A., 2017. Mapping Arctic Coastal Ecosystems with High Resolution Optical Satellite Imagery Using a Hybrid Classification Approach. Can. J. Remote Sens. 43 (6), 513–527.

Danielczuk, M., Matl, M., Gupta, S., Li, A., Lee, A., Mahler, J., Goldberg, K., 2019. Segmenting unknown 3d objects from real depth images using mask r-cnn trained on synthetic data. In: 2019 International Conference on Robotics and Automation (ICRA). IEEE, pp. 7283–7290.

Ehlers, M., Klonus, S., Johan Ã…strand, P.R., Rosso, P., 2010. Multi-sensor image fusion for pansharpening in remote sensing. Int. J. Image Data Fusion, 1, 1, 25–45.

Imagine, E.R.D.A.S., 2015. ERDAS imagine electronic help document. Hexagon Geospatial, Madison, Alabama, USA.

Everett, K.R., 1980. Landforms. In: Geobotanical Atlas of the Prudhoe Bay Region, Alaska. CRREL Report 80-14. In: Walker, D.A., Everett, K.R., Webber, P.J., Brown, J. (Eds.), U.S. Army Corps of Engineers, Cold Regions Research and Engineering Laboratory, Hanover, NH, pp. 14–19.

Farquharson, L.M., Romanovsky, V.E., Cable, W.L., Walker, D.A., Kokelj, S.V., Nicolsky, D., 2019. Climate Change Drives Widespread and Rapid Thermokarst Development in Very Cold Permafrost in the Canadian High Arctic. Geophys. Res. Lett. 46 (12), 6681–6689.

Fernandez, D., Wilkins, A.J., 2008. Uncomfortable Images in Art and Nature. Perception 37 (7), 1098–1113.

French, H.M., 2018. The Periglacial Environment, 4th ed. John Wiley and Sons Ltd., Chichester, UK, p. (515 pp.)..

Frost, G.V., Christopherson, T., Jorgenson, M.T., Liljedahl, A.K., Macander, M.J., Walker, D.A., Wells, A.F., 2018. Regional Patterns and Asynchronous Onset of Ice-Wedge Degradation since the Mid-20th Century in Arctic Alaska. Remote Sens. 10, 1312.

Gangkofner, U.G., Pradhan, P.S., Holcomb, D.W., 2008. Optimizing the High-Pass Filter Addition Technique for Image Fusion. Photogramm. Eng. Remote Sens. 74 (9), 1107–1118.

Garcia, J.A., Rodriguez-Sánchez, R., Fdez-Valdivia, J., Toet, A., 2012. Visual efficiency of image fusion methods. Int. J. Image Data Fusion 3 (1), 39–69.

Gharbia, R., El Baz, A.H., Hassanien, A.E., Tolba, M.F., 2014. Remote Sensing Image Fusion Approach Based on Brovey and Wavelets Transforms. Springer International Publishing, Cham, pp. 311–321.

Ghassemian, H., 2016. A review of remote sensing image fusion methods. Inform. Fusion 32, 75–89.

Goforth, M.A., 1998. Multispectral image sharpening with multiresolution analysis and the MTF. Aerospace/Defense Sens. Controls 3372, SPIE.

Gonçalves, B.C., Spitzbart, B., Lynch, H.J., 2020. SealNet: A fully-automated pack-ice seal detection pipeline for sub-meter satellite imagery. Remote Sens. Environ. 239, 111617.

Guirado, E., Tabik, S., Alcaraz-Segura, D., Cabello, J., Herrera, F., 2017. Deep-learning Versus OBIA for Scattered Shrub Detection with Google Earth Imagery: Ziziphus lotus as Case Study. Remote Sens. 9 (12), 1220.

Guirado, E., Tabik, S., Rivas, M.L., Alcaraz-Segura, D., Herrera, F., 2019. Whale counting in satellite and aerial images with deep learning. Sci. Rep. 9 (1), 14259.

He, K., Gkioxari, G., DollÃ¡r, P. and Girshick, R., 2017. Mask r-cnn. In: Proceedings of the IEEE international conference on computer vision, pp. 2961–2969.

Hinzman, L.D., Bettez, N.D., Bolton, W.R., Chapin, F.S., Dyurgerov, M.B., Fastie, C.L., Griffith, B., Hollister, R.D., Hope, A., Huntington, H.P., Jensen, A.M., Jia, G.J., Jorgenson, T., Kane, D.L., Klein, D.R., Kofinas, G., Lynch, A.H., Lloyd, A.H., McGuire, A.D., Nelson, F.E., Oechel, W.C., Osterkamp, T.E., Racine, C.H., Romanovsky, V.E., Stone, R.S., Stow, D.A., Sturm, M., Tweedie, C.E., Vourlitis, G.L., Walker, M.D., Walker, D.A., Webber, P.J., Welker, J.M., Winker, K.S., Yoshikawa, K., 2005. Evidence and Implications of Recent Climate Change in Northern Alaska and Other Arctic Regions. Clim. Change 72 (3), 251–298.

Hjort, J., Karjalainen, O., Aalto, J., Westermann, S., Romanovsky, V.E., Nelson, F.E., EtzelmÃ¼ller, B., Luoto, M. 2018. Degrading permafrost puts Arctic infrastructure at risk by mid-century. Nat. Commun., 9, 1, 5147.

Huang, L., Luo, J., Lin, Z., Niu, F., Liu, L., 2020. Using deep learning to map retrogressive thaw slumps in the Beiluhe region (Tibetan Plateau) from CubeSat images. Remote Sens. Environ. 237, 111534.

Hugelius, G., Bockheim, J.G., Camill, P., Elberling, B., Grosse, G., Harden, J.W., Johnson, K., Jorgenson, T., Koven, C.D., Kuhry, P., 2013. A new data set for estimating organic carbon storage to 3 m depth in soils of the northern circumpolar permafrost region. Earth Syst. Sci. Data (Online) 5 (2).

Hussey, K.M., Michelson, R.W., 1966. Tundra relief features near Point Barrow. Alaska. Arctic 19 (2), 162–184.

Jiang, Z.J., Von Ness, K., Loisel, J., Wang, Z., 2019. ArcticNet: A Deep Learning Solution to Classify Arctic Wetlands, posarXiv:1906.00133v1.

Jorgenson, M.T., Grosse, G., 2016. Remote sensing of landscape change in permafrost regions. Permafrost Periglac. Process. 27 (4), 324–338.

Jorgenson, M.T., Kanevskiy, M.Z., Shur, Y., Moskalenko, N.G., Brown, D.R.N., Wickland, K., Striegl, R., 2015. Koch Ground ice dynamics and ecological feedbacks control ice-wedge degradation and stabilization. JGR Earth Surf. 120 (11), 2280–2297.

Jones, B.M., Grosse, G.D., A.C., Arp, C.D., Jones, M.C., Anthony, K.W., Romanovsky, V. E., 2011. Modern thermokarst lake dynamics in the continuous permafrost zone, northern Seward Peninsula, Alaska. J. Geophys. Res.: Biogeosci., 116, G2.

Jones, B.M., Grosse, G., Arp, C.D., Miller, E., Liu, L., Hayes, D.J., Larsen, C.F., 2015. Recent Arctic tundra fire initiates widespread thermokarst development. Sci. Rep. 5, 15865.

Jones, B.M., Farquharson, L.M., Baughman, C.A., Buzard, R.M., Arp, C.D., Grosse, G., Bull, D.L., Günther, F., Nitze, I., Urban, F., Kasper, J.L., 2018. A decade of remotely sensed observations highlight complex processes linked to coastal permafrost bluff erosion in the Arctic. Environ. Res. Lett. 13 (11).

Jones, M.K.W., Pollard, W.H., Jones, B.M., 2019. Rapid initialization of retrogressive thaw slumps in the Canadian high Arctic and their response to climate and terrain. Environ. Res. Lett. 14 (5).

Jorgenson, M.T., Shur, Y.L., Pullman, E.R., 2006. Abrupt increase in permafrost degradation in Arctic Alaska. Geophys. Res. Lett. 33 (2).

Kanevskiy, M., Shur, Y., Jorgenson, T., Brown, D.R.N., Moskalenko, N., Brown, J., Walker, D.A., Raynolds, M.K., Buchhorn, M., 2017. Degradation and stabilization of ice wedges: Implications for assessing risk of thermokarst in northern Alaska. Geomorphology 297, 20–42.

Karathanassi, V., Kolokousis, P., Ioannidou, S., 2007. A comparison study on fusion methods using evaluation indicators. Int. J. Remote Sens. 28 (10), 2309–2341.

Kim, M., Holt, J.B., Madden, M., 2011. Comparison of Global- and Local-scale Pansharpening for Rapid Assessment of Humanitarian Emergencies. Photogramm. Eng. Remote Sens. 77 (1), 51–63.
Klonus, S., Ehlers, M., 2007. Image Fusion Using the Ehlers Spectral Characteristics Preservation Algorithm. GIScience & Remote Sens. 44 (2), 93–116.
Laben, C.A., Bernard, V., Brower, W., 2000. Process for enhancing the spatial resolution of multispectral imagery using pan-sharpening. United States Patent Application No. 6,011,875.
Lafreniere, M., Lamoureux, S., 2019. Effects of changing permafrost conditions on hydrological processes and fluvial fluxes. Earth-Sci. Rev., 191.
Lang, S., Baraldi, A., Tiede, D., Hay, G., Blaschke, T., 2018. Towards a (GE) OBIA 2.0 manifestoâ€“Achievements and open challenges in information & knowledge extraction from big Earth data. Proceedings of the GEOBIA.
Lara, M.J., McGuire, A.D., Euskirchen, E.S., Tweedie, C.E., Hinkel, K.M., Skurikhin, A.N., Romanovsky, V.E., Grosse, G., Bolton, W.R., Genet, H., 2015. Polygonal tundra geomorphological change in response to warming alters future CO_2 and CH_4 flux on the Barrow Peninsula. Glob. Change Biol. 21 (4), 1634–1651.
LeCun, Y., Bengio, Y., Hinton, G., 2015. Deep learning. Nature 521 (7553), 436–444.
Leffingwell, E.de K., 1915. Ground-ice wedges, the dominant form of ground-ice on the north coast of Alaska. J. Geol. 23, 635–654.
Levenstein, B., Culp, J.M., Lento, J., 2018. Sediment inputs from retrogressive thaw slumps drive algal biomass accumulation but not decomposition in Arctic streams, NWT. Freshwater Biol. 63 (10), 1300–1315.
Lewkowicz, A.G., Way, R.G., 2019. Extremes of summer climate trigger thousands of thermokarst landslides in a High Arctic environment. Nat. Commun. 10 (1), 1329.
Li, S., Kang, X., Fang, L., Hu, J., Yin, H., 2017. Pixel-level image fusion: A survey of the state of the art. Inform. Fusion 33, 100–112.
Liljedahl, A.K., Boike, J., Daanen, R.P., Fedorov, A.N., Frost, G.V., Grosse, G., Hinzman, L.D., Iijma, Y., Jorgenson, J.C., Matveyeva, N., Necsoiu, M., Raynolds, M. K., Romanovsky, V.E., Schulla, J., Tape, K.D., Walker, D.A., Wilson, C.J., Yabuki, H., Zona, D., 2016. Pan-Arctic ice-wedge degradation in warming permafrost and its influence on tundra hydrology. Nat. Geosci. 9, 312–318.
Lin, T.Y.; Dollár, P.; Girshick, R.; He, K.; Hariharan, B.; Belongie, S. Feature pyramid networks for object detection. In: Proceedings of the 2017 IEEE Conference on Computer Vision and Pattern Recognition (CVPR), Honolulu, HI, USA, 21–26 July 2017; IEEE: Piscataway, NJ, USA, 2017, http://doi.org/10.1109/CVPR.2017.106.
Lindgren, E.J., Kilston, S., 1996. Projective pan sharpening algorithm. SPIE's 1996 International Symposium on Optical Science, Engineering, and Instrumentation, 2818. SPIE.
Long, J., Shelhamer, E., Darrell, T., 2015. Fully convolutional networks for semantic segmentation. In: Proceedings of the 2015 IEEE Conference on Computer Vision and Pattern Recognition (CVPR), Boston, MA, USA, 7–12 June 2015; IEEE: Piscataway, NJ, USA, 2015, http://doi.org/10.1109/CVPR.2015.7298965.
Ma, L., Liu, Y., Zhang, X., Ye, Y., Yin, G., Johnson, B.A., 2019. Deep learning in remote sensing applications: A meta-analysis and review. ISPRS J. Photogramm. Remote Sens. 152, 166–177.
Mackay, J.R., 1984. The direction of ice-wedge cracking in permafrost: downward or upward? Can. J. Earth Sci. 21 (5), 516–524.
Melvin, A.M., Larsen, P., Boehlert, B., Neumann, J.E., Chinowsky, P., Espinet, X., Martinich, J., Baumann, M.S., Rennels, L., Bothner, A., Nicolsky, D.J., 2017. Climate change damages to Alaska public infrastructure and the economics of proactive adaptation. Proc. Natl. Acad. Sci. USA 114 (2), 122–131.
Meng, X., Shen, H., Li, H., Zhang, L., Fu, R., 2019. Review of the pansharpening methods for remote sensing images based on the idea of meta-analysis: Practical discussion and challenges. Inform. Fusion 46, 102–113.
Mora, C., Vieira, G.A., Pina, P., Lousada, M., Christiansen, H.H., 2015. Land cover classification using high-resolution aerial photography in Adventdalen, Svalbard. Geografiska Annaler: Ser. A, Phys. Geogr. 97 (3), 473–488.
Muster, S., Langer, M., Heim, B., Westermann, S., Boike, J., 2012. Land cover classification of Samoylov Island and Landsat subpixel water cover of Lena River Delta, Siberia, with links to ESRI grid files, Supplement to: Muster, S et al. (2012): Subpixel heterogeneity of ice-wedge polygonal tundra: a multi-scale analysis of land cover and evapotranspiration in the Lena River Delta, Siberia. Tellus Ser. B-Chem. Phys. Meteorol. 64, 17301. https://doi.org/10.3402/tellusb.v64i0.17301), PANGAEA.
Nikolakopoulos, K.G., 2008. Comparison of nine fusion techniques for very high resolution data. Comparison of nine fusion techniques for very high resolution data, 74, 5, 647–660.
Nitze, I., Grosse, G., Jones, B.M., Romanovsky, V.E., Boike, J., 2018. Remote sensing quantifies widespread abundance of permafrost region disturbances across the Arctic and Subarctic. Nat. Commun. 9 (1), 5423.
O'Shea, R.P., Blackburn, S.G., Ono, H., 1994. Contrast as a depth cue. Vision Res. 34 (12), 1595–1604.
Pachauri, R.K., Allen, M.R., Barros, V.R., Broome, J., Cramer, W., Christ, R., Church, J.A., Clarke, L., Dahe, Q., Dasgupta, P., 2014. Climate change 2014: synthesis report. Contribution of Working Groups I, II and III to the fifth assessment report of the Intergovernmental Panel on Climate Change. Ipcc.
Padwick, C., Deskevich, M., Pacifici, F., Smallwood, S., 2010. Worldview-2 pansharpening. ASPRS 2010 Annual Conference, San Diego, California, p. 14.
Péwé, T.L., 1975. Quaternary geology of Alaska. US Geol. Surv. Prof. Pap. 835, 145 pp.
Pohl, C., Van Genderen, J.L., 1998. Multisensor image fusion in remote sensing: concepts, methods and applications. Int. J. Remote Sens. 19 (5), 823–854.
Pradhan, P.S., King, R.L., Younan, N.H., Holcomb, D.W., 2006. Estimation of the Number of Decomposition Levels for a Wavelet-Based Multiresolution Multisensor Image Fusion. IEEE Trans. Geosci. Remote Sens. 44 (12), 3674–3686.
Ranchin, T., Wald, L., 2000. Fusion of high spatial and spectral resolution images: the ARSIS concept and its implementation. Photogramm. Eng. Remote Sens. 66 (1), 49e61.
Ranchin, T., Aiazzi, B., Alparone, L., Baronti, S., Wald, L., 2003. Image fusion–the ARSIS concept and some successful implementation schemes. ISPRS J. Photogramm. Remote Sens. 58 (1–2), 4–18.
Raynolds, M.K., Walker, D.A., Ambrosius, K.J., Brown, J., Everett, K.R., Kanevskiy, M., Kofinas, G.P., Romanovsky, V.E., Shur, Y., Webber, P.J., 2014. Cumulative geoecological effects of 62 years of infrastructure and climate change in ice-rich permafrost landscapes, Prudhoe Bay Oilfield, Alaska. Global Change Biol. 20 (4), 1211–1224.
Raynolds, M.K., Walker, D.A., Balser, A., Bay, C., Campbell, M., Cherosov, M.M., DaniÃ«ls, F.J.A., Eidesen, P.B., Ermokhina, K.A., Frost, G.V., Jedrzejek, B., Jorgenson, M.T., Kennedy, B.E., Kholod, S.S., Lavrinenko, I.A., Lavrinenko, O.V., MagnÃ°sson, B.Ã.r., Matveyeva, N.V., MetÃ°salemsson, S., Nilsen, L., Olthof, I., Pospelov, I.N., Pospelova, E.B., Pouliot, D., Razzhivin, V., Schaepman-Strub, G., Å ibÃk, J., Telyatnikov, M.Y., Troeva, E., 2019. A raster version of the Circumpolar Arctic Vegetation Map (CAVM). Remote Sens. Environ., 232, 111297.
Ren, S., He, K., Girshick, R., Sun, J., 2015. Faster r-cnn: Towards real-time object detection with region proposal networks. Adv. Neural Inf. Process. Syst. 91–99.
Schuur, E.A.G., Mack, M.C., 2018. Ecological Response to Permafrost Thaw and Consequences for Local and Global Ecosystem Services: Annual Review of Ecology. Evol., Systemat. 49 (1), 279–301.
Shahdoosti, H.R., Ghassemian, H., 2016. Combining the spectral PCA and spatial PCA fusion methods by an optimal filter. Inform. Fusion 27, 150–160.
Shur, Y.L., Jorgenson, M.T., 2007. Patterns of permafrost formation and degradation in relation to climate and ecosystems. Permafrost Periglac. Process. 18 (1), 7–19.
Skurikhin, A.N., Gangodagamage, C., Rowland, J.C., Wilson, C.J., 2013. Arctic tundra ice-wedge landscape characterization by active contours without edges and structural analysis using high-resolution satellite imagery. Remote Sens. Lett. 4 (11), 1077–1086.
Steedman, A.E., Lantz, T.C., Kokelj, S.V., 2017. Spatiotemporal variation in high centre polygons and ice wedge melt ponds, Tuktoyaktuk coastlands, Northwest Territories. Permafrost Periglacial Processes 28 (1), 66–78.
Sudmanns, M., et al., 2019. Big Earth data: disruptive changes in Earth observation data management and analysis? Int. J. Digital Earth 1–19.
Towns, J., Cockerill, T., Dahan, M., Foster, I., Gaither, K., Grimshaw, A., Hazlewood, V., Lathrop, S., Lifka, D., Peterson, G.D., Roskies, R., Scott, J.R., Wilkins-Diehr, N., 2014. XSEDE: Accelerating Scientific Discovery. Comput. Sci. Eng. 16 (5), 62–74.
Tsushima, Y., Komine, K., Sawahata, Y., Hiruma, N., 2014. Higher resolution stimulus facilitates depth perception: MT+ plays a significant role in monocular depth perception. Sci. Rep. 4, 6687.
Tsushima, Y., Komine, K., Sawahata, Y., Morita, T., 2016. Undetectable Changes in Image Resolution of Luminance-Contrast Gradients Affect Depth Perception. Front. Psychol. 7, 242.
Turetsky, M.R., Abbott, B.W., Jones, M.C., Anthony, K.W., Olefeldt, D., Schuur, E.A.G., Koven, C., McGuire, A.D., Grosse, G., Kuhry, P., 2019. Permafrost collapse is accelerating carbon release. Nature Publishing Group.
Ulrich, M., Hauber, E., Herzschuh, U., HÃ¤rtel, S., and Schirrmeister, L., 2011, Polygon pattern geomorphometry on Svalbard (Norway) and western Utopia Planitia (Mars) using high-resolution stereo remote-sensing data. Geomorphology, 134, no. 3-4, 197–216.
van Everdingen, R.O., (edit) 1998. Multi-language glossary of permafrost and related ground-ice terms. Univ. of Calgary Press: Calgary.
van der Sluijs, J., Kokelj, S., Fraser, R., Tunnicliffe, J., Lacelle, D., 2018. Permafrost Terrain Dynamics and Infrastructure Impacts Revealed by UAV Photogrammetry and Thermal Imaging. Remote Sens. 10 (11), 1734.
Vannucci, M., Pia Viggiano, M., Argenti, F., 2001. Identification of spatially filtered stimuli as function of the semantic category. Cognit. Brain Res. 12 (3), 475–478.
Vijayaraj, V., Nicolas, H.Y., Charles, G.O.H., 2006. Quantitative analysis of pansharpened images. Opt. Eng. 45 (4), 046202.
Vincent, W.F., Lemay, M.L., Allard, M., 2017. Arctic permafrost landscapes in transition: towards an integrated Earth system approach. Arct. Sci. 3 (2), 39–64.
Wald, L., 2000. Quality of high resolution synthesised images: Is there a simple criterion ? In: Ranchin, T., Wald, L. (Eds.), Fusion of Earth data: merging point measurements, raster maps and remotely sensed images. SEE/URISCA, Nice, France, Sophia Antipolis, France, p. 166.
Wald, L., 2002. Data fusion: Definitions and architectureseFusion of images of different spatial resolutions. Les Presses, Ecole des Mines de Paris, Paris, France, p. 200.
Witharana, C., Civco, D.L., 2012. Evaluating remote sensing image fusion algorithms for use in humanitarian crisis management. SPIE Remote Sens. 8538, SPIE. 375.
Witharana, C., Civco, D.L., Meyer, T.H., 2013. Evaluation of pansharpening algorithms in support of earth observation based rapid-mapping workflows. Appl. Geogr. 37, 63–87.
Witharana, C., Civco, D.L., Meyer, T.H., 2014. Evaluation of data fusion and image segmentation in earth observation based rapid mapping workflows. ISPRS J. Photogramm. Remote Sens. 87, 1–18.
Witharana, C., Lynch, H., 2016. An Object-Based Image Analysis Approach for Detecting Penguin Guano in very High Spatial Resolution Satellite Images. Remote Sens. 8 (5).
Witharana, C., LaRue, M.A., Lynch, H.J., 2016. Benchmarking of data fusion algorithms in support of earth observation based Antarctic wildlife monitoring. ISPRS J. Photogramm. Remote Sens. 113, 124–143.
Yakhdani, M.F., Azizi, A., 2010. Quality assessment of image fusion techniques for multisensor high resolution satellite images (case study: IRS-p5 and IRS-p6 satellite images). In: W. W. and B. Székely (Editors), ISPRS TC VII Symposium – 100 Years ISPRS. IAPRS, Vienna, Austria, pp. Part7B.

Yang, B., Kim, M., Madden, M., 2012. Assessing Optimal Image Fusion Methods for Very High Spatial Resolution Satellite Images to Support Coastal Monitoring. GIScience Remote Sens. 49 (5), 687–710.
Zhang, L., Zhang, L., Du, B., 2016. Deep Learning for Remote Sensing Data: A Technical Tutorial on the State of the Art. IEEE Geosci. Remote Sens. Mag. 4 (2), 22–40.
Zhang, W., Witharana, C., Liljedahl, A., Kanevskiy, M., 2018. Deep convolutional neural networks for automated characterization of arctic ice-wedge polygons in very high spatial resolution aerial imagery. Remote Sens. 10 (9), 1487.
Zhang, R., Cheng, C., Zhao, X., Li, X., 2019, Multiscale Mask R-CNNâ€“Based Lung Tumor Detection Using PET Imaging: Molecular imaging. 18, 1536012119863531.
Zhang, Y., 2002. A new automatic approach for effectively fusing Landsat as well as IKONOS images. IEEE Trans. Geosci. Remote Sens. 2429–2431.